NASA TECHNICAL NOTE

NASA TN D-7729

NASA TN D-7729

(NASA-TN-D-7729) A STUDY OF THE POSSIBLE CHARACTERISTICS OF A LOW-ALTITUDE ELECTRON LAYER IN THE MARTIAN ATMOSPHERE (NASA) 58 p HC $3.75 CSCL 03B
N74-35264
Unclas
H1/30 52415

A STUDY OF THE POSSIBLE CHARACTERISTICS OF A LOW-ALTITUDE ELECTRON LAYER IN THE MARTIAN ATMOSPHERE

by H. Andrew Wallio

Langley Research Center
Hampton, Va. 23665

NATIONAL AERONAUTICS AND SPACE ADMINISTRATION • WASHINGTON, D. C. • OCTOBER 1974

1. Report No. NASA TN D-7729	2. Government Accession No.	3. Recipient's Catalog No.
4. Title and Subtitle A STUDY OF THE POSSIBLE CHARACTERISTICS OF A LOW-ALTITUDE ELECTRON LAYER IN THE MARTIAN ATMOSPHERE		5. Report Date October 1974
		6. Performing Organization Code
7. Author(s) H. Andrew Wallio		8. Performing Organization Report No. L-9600
9. Performing Organization Name and Address NASA Langley Research Center Hampton, Va. 23665		10. Work Unit No. 185-47-91-06
		11. Contract or Grant No.
12. Sponsoring Agency Name and Address National Aeronautics and Space Administration Washington, D.C. 20546		13. Type of Report and Period Covered Technical Note
		14. Sponsoring Agency Code

15. Supplementary Notes Most of the information presented herein is a revision of material contained in a thesis entitled "The Characteristics of a Possible Low Altitude Electron Layer in the Martian Atmosphere" submitted to the School of Engineering and Applied Science of the George Washington University in December 1973 in partial satisfaction of the requirements for the degree of Master of Science.

16. Abstract

The apparent diurnal Martian surface pressure variation, as deduced from radio occultation experiments, is discussed and explained as possibly arising from the effect of a low-altitude electron layer. Possible source and loss mechanisms for the low-altitude electron layer are presented and discussed. Time-dependent differential equations describing the electron layer are derived and than integrated to investigate the electron distribution resulting from several processes that might occur in the atmosphere. It is concluded that the source mechanism is the sublimation of alkali atoms from a permanent dust layer (a dust layer of 0.2-μm particles of number density 9 cm^{-3} is sufficient), and that the dominant loss process must involve CO_2 clustering about the alkali atoms. By use of these processes, an electron layer is developed which would explain the apparent diurnal surface-pressure variation.

17. Key Words (Suggested by Author(s)) Alkali atoms Low-altitude electron layer Martian atmosphere		18. Distribution Statement Unclassified – Unlimited STAR Category 30	
19. Security Classif. (of this report) Unclassified	20. Security Classif. (of this page) Unclassified	21. No. of Pages 56	22. Price* $3.75

*For sale by the National Technical Information Service, Springfield, Virginia 22151

A STUDY OF THE POSSIBLE CHARACTERISTICS OF A LOW-ALTITUDE ELECTRON LAYER IN THE MARTIAN ATMOSPHERE[1]

By H. Andrew Wallio
Langley Research Center

SUMMARY

The apparent diurnal Martian surface pressure variation, as deduced from radio occultation experiments, is discussed and explained as possibly arising from the effect of a low-altitude electron layer. Possible source and loss mechanisms for the low-altitude electron layer are presented and discussed. Time-dependent differential equations describing the electron layer are derived and then integrated to investigate the electron distribution resulting from several processes that might occur in the atmosphere. It is concluded that the source mechanism is the sublimation of alkali atoms from a permanent dust layer (a dust layer of 0.2-μm particles of number density 9 cm^{-3} is sufficient), and that the dominant loss process must involve CO_2 clustering about the alkali atoms. By use of these processes, an electron layer is developed which would explain the apparent diurnal surface-pressure variation.

INTRODUCTION

Since 1965, there have been four U.S. planetary space probes used in the exploration of the planet Mars. These spacecraft were used to gather data concerning the physical properties of the planet; one of the primary objectives of the research was the determination of the physical properties of the Martian atmosphere. These properties were examined by techniques of visual imagery (refs. 1 to 3), infrared spectroscopy (refs. 4 to 6), infrared radiometry (refs. 7 and 8), ultraviolet spectrometry (refs. 9 to 12), and radio occultation (refs. 13 to 19).

Analyses of radio occultation data from the U.S. Mariner spacecraft have produced a considerable amount of information on both the neutral atmosphere and ionosphere of

---

[1] Most of the information presented herein is a revision of material contained in a thesis entitled "The Characteristics of a Possible Low Altitude Electron Layer in the Martian Atmosphere" submitted to the School of Engineering and Applied Science of the George Washington University in December 1973 in partial satisfaction of the requirements for the degree of Master of Science.

Mars. Data from a single occultation entry and exit were obtained from each of the flyby missions of Mariner 4 (1965), 6 (1969), and 7 (1969), and data from a large number of occultations of the Mariner 9 (1971) orbiter have greatly extended the latitudinal, longitudinal, and diurnal coverage of the planet.

On the basis of the currently available analysis of the Mariner radio occultation data (refs. 16 and 17), there are some indications of apparently systematically higher surface pressures on the nightside of Mars than on the dayside. This difference is approximately 1 mb or roughly 20 percent of the total pressure. These indications of an apparent diurnal variation in surface pressure might be explained by either a variation in topography at the occultation location or by some sort of diurnal process occurring in the atmosphere. This paper will discuss one atmospheric diurnal process that might explain the radio occultation results.

In a radio occultation experiment, as the spacecraft passes behind the planet, the atmosphere acts as a lens to the radio ray and changes the apparent motion of the spacecraft. The changes in motion of the spacecraft are measured by the change in frequency of the received radio ray (Doppler signal). After subtracting the predicted change in spacecraft motion from the measured Doppler change, the difference or residual is used to deduce the atmospheric density. It has been shown that there are interpretation ambiguities inherent in the reconstruction of atmospheric properties from single-frequency radio occultation data. (See ref. 20.) This ambiguity arises from the fact that the deduced refractivity can be composed of both a positive component (due to the neutral atmosphere which causes an apparent motion away from the observer) and a negative component (due to the presence of free electrons which cause an apparent motion toward the observer). Thus, a single-frequency occultation measurement can be represented by one equation with two unknowns which cannot be solved for the effects of the two components separately. Because of this interpretation ambiguity, numerous atmospheric models (representing different atmospheric states) can be developed that will produce the refractivity profile obtained from any single-frequency radio occultation experiment. One atmospheric model that accounts for the apparent pressure disparity includes a time-dependent low-altitude electron layer in the dayside atmosphere. (See ref. 21.)

The properties of a planetary atmosphere and ionosphere vary with altitude, latitude, longitude, and the local time of day. A low-altitude electron layer will possess similar variations. This paper will discuss an atmospheric model that includes an electron layer and will develop equations to describe the altitude and time variations of the layer. To do this, the simplified (no transport) time-dependent electron density continuity equation is normalized and nondimensionalized for ease of handling. The resulting first-order nonlinear differential equation is integrated to give diurnal electron density profiles as a function of various absorption and recombination coefficients. The development of these models is somewhat the reverse of that associated with the classical Chapman electron-layer theory. In that theory, the atmospheric properties are known and the resulting electron layer is determined. In the present case, the magnitude and functional form of the electron layer at a specific geographic location and local time is specified by the difference between the refractivity resulting from the neutral atmosphere and the refractivity as measured by radio occultation. Knowledge of the electron distribution then allows the distribution of the ionizable constituent to be determined. The recombination and the absorption coefficients in the atmospheric model are empirically adjusted until an acceptable ionizing constituent model which produces the specified electron distribution results.

SYMBOLS

A	symbol for alkali atom
B	coefficient used to define alkali height distribution
$\vec{B}$	magnetic induction vector
C	coefficient used to define alkali height distribution
d	distance along ionization path (defined in fig. 5)
$\vec{E}$	electric field vector
e	electron and charge on electron
f	dynamical flattening coefficient; also frequency of radio waves
G(t)	dummy variable
g	acceleration due to Mars gravity
H	scale height in atmosphere
$\vec{H}$	magnetic intensity vector
h	altitude along ionization path; also Planck's constant (eqs. (24) and (25))

I	intensity of sunlight along ionization path
I_0	intensity of sunlight outside atmosphere
i_p	impact parameter (defined in fig. 5)
$\vec{J}$	electron current vector
K	constant used to define alkali number density
K_{mn}	rate coefficient for reaction mn
L	a term which accounts for loss of electrons
l	length along ionization path
M	third particle (probably dust)
m	mass of electron
N	refractivity, $(\mu - 1) \times 10^6$
N_c	composite refractivity in atmosphere
N_e	component of refractivity due to electrons
N_n	component of refractivity due to neutral particles
n_A	number density of alkali atoms
n_{CO_2}	number density of CO_2 molecules
n_e	number density of electrons
n_n	number density of neutral molecules
P	probability of ionization
p_e	rate of production of electrons

p_i	measured surface pressure
p_0	base surface pressure
Q	absorption coefficient
R	gas constant
R_p	radius of planet
T	atmospheric gas kinetic temperature
t	time
$\vec{V}$	atmospheric wind velocity
$\vec{v}$	electron velocity due to electric field (see appendix)
W	variable in equation (34)
X	variable of integration
Z	altitude in atmosphere
α	electron recombination coefficient
δ	number of electrons released per captured photon
ϵ_c	dielectric constant of composite atmosphere
ϵ_n	dielectric constant of neutral atmosphere
ϵ_0	dielectric constant of free space
λ	wavelength of radiation
λ_1,λ_2	angle along ionization path (fig. 5)
μ	index of refraction

ν	frequency of radiation
σ	cross section of CO_2 absorption; conductivity of electron gas
ϕ	local time (hour angle) measured from noon
χ	solar zenith angle
ω	angular frequency of radio ray

Subscripts:

A	alkali atoms
c	composite atmosphere
e	electrons
i	an ith measurement
max	maximum
n	the neutral atmosphere
0	a base level

RADIO OCCULTATION AND THE MARTIAN ATMOSPHERE

The radio occultation occurs as a spacecraft passes behind a planet as viewed from the tracking station. The radio signal between the spacecraft and tracking station is changed by passing through the atmosphere of the planet being studied. By making certain assumptions about the atmosphere, the position of the spacecraft, and the propagation paths, the change in the received radio frequency (Doppler) as the radio ray passes through the atmosphere can be related to the index of refraction of the atmosphere. Since the index of refraction μ of most gases is numerically very close to unity, the quantity generally used in describing the atmosphere is the refractivity unit. The refractivity is related to the index of refraction as

$$N \equiv (\mu - 1)10^6$$

Figure 1 is a sketch of a typical profile of refractivity as a function of altitude for the atmosphere of Mars (based on ref. 13). Plots such as figure 1 are the usual output of radio occultation experiments, and it is these plots that form the basis for the inference of atmospheric properties. The negative refractivity peak which occurs at 135 km on the dayside profile is attributed to free electrons resulting from photoionization processes involving CO_2 in the Martian atmosphere. If there are at most a very small number of low mass ions present (a reasonable assumption for the atmosphere of Mars), the number of free electrons is simply related to the negative refractivity by a linear equation.

The lower positive peak is assumed, by most authors, to be caused only by the neutral atmosphere. The relationship between the refractivity and the properties of the neutral atmosphere is more complex than that for electrons since there can be several gases which contribute to the refractivity and only one equation relating them. Therefore, the exact gas composition must either be known or assumed, whereas the refractivity profile is used to determine the molecular number density. The molecular number density is used together with the hydrostatic equation and the perfect gas law to determine the temperature distribution in the atmosphere. The pressure variation in the atmosphere can be obtained by either integrating the number density in the hydrostatic equation or by using the temperature distribution in the perfect gas law.

The peak dayside electron density, as deduced from the Mariner radio occultation, occurs at about 135 km with a magnitude of approximately 1.6×10^5 electrons per cm^3. The deduced atmospheric surface temperatures vary from 141 K to 272 K, about 240 K being the average dayside surface temperature and about 160 K being the average nightside surface temperature. The deduced lapse rate in the atmosphere varies from 0 to 3.8 K/km, a large number of measurements implying a near isothermal atmosphere, and almost all measurements having a lapse rate of less than one-half the theoretical adiabatic lapse rate (5 K/km). (See ref. 19.) (These small temperature gradients are the basis of using, in the following sections, the approximation that the atmosphere is isothermal near the surface. The error in pressure obtained by using an isothermal approximation over a height of 10 km will be no larger than about 3 percent at 10 km.) The deduced Martian surface pressures vary from 2.5 mb to 10.8 mb, the average surface pressure being from 4.7 to 6.1 mb, depending upon the surface that is taken to be representative of the mean planet surface. (1 bar = 1×10^5 Pa.)

DESCRIPTION OF APPARENT DIURNAL VARIATION IN SURFACE PRESSURE

On the basis of the currently available analysis of the Mariner radio occultation data (refs. 16 to 18), there are indications of apparently systematically higher surface pressures on the nightside of Mars than on the dayside. It is difficult to examine the published occultation surface pressures as a group, since the data occurs at different altitudes, places, times of day, and times of year. To compare the data as a group, the effects of different altitudes and temperatures in the atmosphere are taken into account, and any of the previously mentioned effects (including season and meteorology) will be assumed to cancel out when group averages are taken.

A reasonable approximation for a Martian equipotential surface can be obtained from the dynamical flattening. (See ref. 22.) An approximation to the equipotential radius as a function of latitude is $R \approx R_{eq}\left[1 - f \sin^2(LAT)\right]$, where R_{eq} is the equatorial radius, f the flattening coefficient, and LAT is the latitude of the point in question. From Mariner 9 orbital analysis (refs. 23 and 24), the flattening coefficient f was measured to be 5.25×10^{-3}, and this value is used in the following analysis.

To allow for the different values of deduced surface temperatures and altitudes associated with each deduced surface pressure, the deduced surface pressures are compared by two methods. The first method is to scale each surface pressure data point to a pressure altitude. The pressure altitude is the altitude in a reference atmosphere at which a given pressure level occurs. As an illustration of this method, assume that the Martian equipotential surface has the same dayside and nightside pressure p_0 at the zero altitude or base surface, then for a deduced pressure p_i, temperature T_i $\left(\text{associated scale height, } H_i = \frac{RT_i}{mg}\right)$, and altitude, Z_i,

$$p_i = p_0 \exp\left(-\frac{Z_i}{H_i}\right)$$

The reference atmosphere is taken to have the same equipotential surface, the same zero altitude pressure p_0, a constant temperature T_0 (and, therefore, scale height H_0) over the entire reference surface. Then, for the same deduced pressure p_i there is a pressure altitude $Z_{0,i}$ such that

$$p_i = p_0 \exp\left(-\frac{Z_{0,i}}{H_0}\right)$$

and therefore, the pressure altitude associated with each p_i, T_i, and Z_i deduced from a radio occultation experiment is defined as

$$Z_{0,i} = \frac{H_0}{H_i} Z_i$$

If the base surface pressure is the same for both the dayside and nightside surface, then the natural log of the pressure data plotted against the pressure altitude should all lie on a straight line (within the measurement accuracy and the assumption of an isothermal atmosphere over the heights in question).

Figure 2 is a plot of pressure against pressure altitude above a geopotential $\left(R_{equator} = 3390\ \text{km},\quad f = 5.25 \times 10^{-3}\right)$ for a set of night (exit) and day (entrance) deduced surface pressures. A reference temperature of 240 K was used and therefore $H_0 = 12$ km and the deduced surface temperature at each data point was used for H_i to calculate the pressure altitude. The line in figure 2 is a reference atmosphere with a base pressure of 6.1 mb and a scale height of 12 km. As can be seen from figure 2, the dayside (entrance) pressure measurements are not very far from the line but the nightside (exit) pressure measurements cluster above the line; this condition implies that the assumption of an equal base surface pressure for both the dayside and the nightside was invalid.

The second way to compare the data is to examine the base surface pressure p_0 by the relation

$$p_0 = p_i \exp\left(+ \frac{Z_i}{H_i}\right)$$

where p_i, Z_i, and H_i are the surface pressure, altitude from the geopotential, and scale height deduced from the radio occultation experiment. Figure 3 is a plot of the calculated base surface pressure against relative time of day for a set of day (entry) and night (exit) measurements referenced to a geopotential. Again the difference between day and night pressure measurements is evident and is approximately 1 mb.

Since it is considered unlikely that a day-night pressure differential of such magnitude (20 percent of the total pressure) could actually be sustained for any appreciable time, some process or combination of processes must be causing the apparent difference. These might be such things as variations in the topography at the occultation location, large variations from a simple geopotential surface (smaller perturbations have been implied in refs. 25 and 26), or some diurnal process occurring in the atmosphere (ref. 21).

Among the possible causes of the apparent diurnal pressure difference, one of the most interesting and least examined is some diurnal process occurring in the lower atmosphere. A most plausible cause of a diurnal process is solar radiation as a driving source for some mechanism in the atmosphere. Solar radiation is responsible for both heating and ionization in the atmosphere. Ionization is precisely the process to examine, since free electrons exhibit a negative refractivity when probed with radio waves.

In order to illustrate how electrons can affect the apparent pressure, it will be necessary to review the discussion from the previous section. Figure 1 is a sketch of a typical dayside (entry) and nightside (exit) refractivity profile obtained from the radio occultation experiment. (See ref. 18.) These refractivity profiles are results of the experiment and are used as the basic data for deriving atmospheric properties. The positive refractivity in the lower atmosphere has been assumed to be caused by the neutral atmosphere. The assumption made by most authors in interpreting the refractivity data is that there are no free electrons below the 50- to 70-km region. Therefore, the smaller positive dayside refractivity is interpreted as a smaller dayside pressure. Harrington et al. (ref. 20) have pointed out that if there are free electrons below 50 km on the dayside, these electrons would contribute a negative component to the refractivity in this region. The observed refractivity would then be a composite of the negative refractivity due to the free electrons and the positive refractivity due to the neutral atmosphere. The observed composite refractivity would then be smaller than that of the actual neutral component of refractivity and, therefore, the pressure deduced from the observed refractivity would be less than the actual atmospheric pressure.

ESTIMATION OF FORM OF ELECTRON LAYER

If it is assumed that the dayside positive section of the lower refractivity profile, as shown in figure 1, is a composite profile of the neutral atmosphere plus an electron layer, then it can be shown that the real part of the index of refraction is (see appendix):

$$\mu_c^2 = \mu_n^2 - n(e^-)^2\left[(2\pi)^2\epsilon_0 m f^2\right]^{-1} \tag{1}$$

where μ_c is the measured composite real index of refraction, μ_n is the real index of refraction of the neutral atmosphere, and the remaining terms are the contribution of the electron layer (where n is the number of electrons, e^- and m are the charge and mass of an electron, ϵ_0 is the dielectric constant of free space, and f is the frequency of the probing radio signal).

Rearranging equation (1) and introducing refractivity $N \equiv (\mu - 1) \times 10^6$

$$N_e = -1 + \left[1 - (1 + N_n)^2 + (1 + N_c)^2\right]^{1/2} \tag{2}$$

where N_e is the refractivity of the electron distribution, N_c is the measured refractivity, and N_n is the refractivity of the neutral atmosphere. Equation (2) can be approximated as (see appendix):

$$N_e \approx N_c - N_n \tag{3}$$

Assuming that the atmosphere is in hydrostatic equilibrium and that the neutral refractivity is proportional to the neutral density (a valid assumption for the low gas density on Mars) results in

$$N_n(Z) = N_n(0) \exp\left(-\frac{Z}{H_n}\right) \tag{4}$$

where Z is the altitude above the geopotential and H_n is the scale height of the neutral atmosphere

$$H_n \equiv Z\left(\int_0^Z \frac{mg}{RT}\,dZ\right)^{-1} \tag{5}$$

By assuming that the deduced nightside surface pressure is more indicative of the actual surface pressure, and by allowing various formulations for H_n, that is, isothermal, constant-temperature gradients, and so forth, many models of electron distributions can be derived. Figure 4 (from ref. 21) is a sketch of electron number density as a function of altitude for several derived electron distribution models. The upper solid curve is the ionosphere that is deduced by radio occultation for most dayside occultations. The lower three curves are possible electron distribution models which would essentially equalize the surface pressure, and which would still yield the same refractivity profile as the refractivity profile observed by the radio occultation experiment. As can be seen from figure 4, these calculated layers all have peak densities of 6 to 8×10^4 electrons per cm^3 and the peak density occurs at altitudes below 15 km. It should also be noted that the calculated electron density profiles are only rough estimates, since the data from which they are calculated consist primarily of published numbers of the pressure at the point of radio occultation and the measured refractivity profiles in the atmosphere (of which very few profiles have been published). To compound the problem there are large differences in the surface pressures, deduced from the same radio occultation data, by different authors.

SOURCE OF PROPOSED ELECTRON LAYER

In the past, Martian ionospheric models have been controversial, and much research has been done on the upper ionosphere of Mars with differing ideas about the ionosphere. (See refs. 13 and 28 to 31.) Although the existence of low (below 50 km) electron layers on Mars has been conjectured (ref. 31) and electron density of the order of 10^4 cm^{-3} peaked at 65 km has been measured (ref. 32), little research has been reported on the lower ionosphere. Whitten et al. (refs. 33 and 34) have studied the lower Martian ionosphere by studying the influx of solar protons and cosmic rays on a CO_2 atmosphere. They concluded that for a quiet Sun the lower ionosphere below 65 km is formed predominately by galactic cosmic rays, is a layer which may have little diurnal variation, and is peaked at approximately 25 to 35 km with a maximum density of the order of 10^3 electrons cm^{-3}.

Since all the efficient channels of electron production involving photochemical processes in gaseous carbon dioxide in the Martian atmosphere have been utilized in theoretical modeling of the ionosphere, the postulated electron layer must come from some other process not involving CO_2 in the atmosphere. Also, since the effect of the electron layer is diurnal, the electron density should exhibit a diurnal variation. If it is assumed that this diurnal variation is driven by sunlight, the source must be able to liberate electrons when exposed to solar ultraviolet radiation. It is known that CO_2 gas absorbs significantly in the 100 to 1700 Å region (ref. 35) and CO_2 gas is completely transparent from about 1800 Å to at least 2100 Å (ref. 36). The Martian atmosphere has very little ozone and therefore there is an ultraviolet window in the 1750 Å to 2100 Å region (ref. 35). Hence, radiation in this wavelength interval can reach the Martian surface. It follows then that the electron source material must release electrons when exposed to radiation in the 1800 Å to 2100 Å region (6.9 eV to 5.9 eV). Based on ionization potentials and abundance criteria, the list of source candidates has been reduced to potassium (ionization potential, 4.3 eV), sodium (5.12 eV), barium (5.19 eV), lithium (5.36 eV), aluminum (5.96 eV), and calcium (6.09 eV). All these materials are cosmically abundant and found in both planetary crustal material and meteoric dust.

This electron source material, alkali metals in the atmosphere, must come from either the top of the atmosphere (meteoric ablation), the bottom of the atmosphere (crustal material raised into the atmosphere by the wind), or a combination of the two methods. It is proposed that the alkali metals sublimate from aerosols or "dust" particles (ref. 37) that have arrived in the atmosphere by one of the methods just mentioned.

Dust and aerosol particles in the Martian atmosphere have been observed and measured by many authors (refs. 2, 35, and 38 to 42). Thin detached haze layers were distinguished in Mariner photographs at altitudes of 5 to 45 km (ref. 43). The presence of dust in the atmosphere was found to be able to account for the fact that measured atmospheric temperatures were considerably warmer than the theoretical temperatures calculated, if radiative equilibrium in the atmosphere is assumed. (See ref. 44.) The presence of a low-altitude dust layer could also account for the observed photolytic stability of the Martian CO_2 atmosphere and in addition this dust brings into agreement the observed and computed profiles of the minor constituents O, O_2, CO, and O_3. (See ref. 45.) In fact, some authors have concluded that there are aerosols permanently present in the Martian atmosphere that absorb solar radiation. (See ref. 46.) This dust would most likely be composed of oxides of Si, Ti, Fe, Mn, Mg, Ca, and Na. (See ref. 47.) The dust in the Martian atmosphere has a measured SiO_2 content of about 60 percent, by weight (ref. 39); and since this is a slightly enhanced silicon content (compared with lunar or chondritic material), the alkaline content will also be enhanced. (See ref. 48.)

The dust could arrive in the atmosphere in either one or both of two ways. First, the dust may be the result of the surface material having been broken up into fine powder by the heating and cooling differences experienced over a Martian day. This powdered surface material could easily be blown into the atmosphere by thermal winds (refs. 49 and 50) or localized dust storms which occur rather frequently (ref. 51). Since 0.2-μm particles would remain in the atmosphere on the order of 2 years, the atmosphere may contain such particles most of the time. (See ref. 52.) Second, the dust could result from the ablation of meteoroids which enter the atmosphere. This idea has been advanced as the source of sodium layers in the Earth's atmosphere (ref. 53) and since Mars is closer to the asteroid belt than Earth, the effect may be even more pronounced for Mars.

MODELING OF ALKALI LAYER

Aerosol layers have been detected in the Earth's lower atmosphere (see refs. 54 to 56). Alkali metal layers have also been measured in the Earth's atmosphere. (See refs. 53 and 57 to 61.) The sodium layer in the Earth's atmosphere has been postulated to come from an aerosol or "dust bank layer" (refs. 61 to 63), or from meteoric material (refs. 37, 53, and 64). The actual photochemical process and distributions in the Earth's atmosphere are not too well understood or modeled, primarily because of the lack of quantitative atmospheric data, lack of laboratory measurements of the physical properties of metal ions and their oxides, and lack of knowledge as to the effects of competing reactions such as CO_2 clustering (ref. 65) and aerosol ion pair annihilation (ref. 66).

It will be assumed that the final Martian alkali number distribution follows roughly the same shape as that found for Earth's sodium distribution (such as shown in ref. 64) and that this distribution can be adequately approximated by the equation

$$n_A(Z) = K \exp\left(-\frac{Z}{C} - Be^{-Z/C}\right) \tag{6}$$

where $n_A(Z)$ is the initial neutral alkali number density as a function of altitude Z. The quantity C can be thought of as a "scale height" for the rate of fall of the upper side of the distribution and B is a dimensionless constant which controls the shape of the lower side of the distribution. Since the scale height observed in the upper side of the Earth's sodium layer is approximately one-half the neutral atmosphere scale height (ref. 60), C was given the value of 6 km (about one-half the Martian neutral atmosphere scale height). The altitude of peak density of the alkali distribution is given by

$$Z(n_{A,max}) = C \log_e B \tag{7}$$

Thus, the value of B was chosen to be 6 in order that the distribution peak occurs at an altitude below 15 km. (For the numbers chosen, the peak occurs at 10.75 km.)

DERIVATION OF TIME-DEPENDENT ELECTRON DISTRIBUTION

The continuity equation relates the change in electron density per unit time to the production, loss, and the divergence, and is given by

$$\frac{\partial n_e}{\partial t} = p_e - L - \nabla \cdot (n_e \vec{v})$$

where n_e is the electron density, p_e is the production rate, L is the loss rate, and $\vec{v}$ is the transport velocity. It will be assumed that the transport terms can be neglected (except for large dust storms or cases of local severe temperature gradients on sloped surfaces, the expected vertical velocities will displace electrons less than one-tenth of the neutral atmosphere scale height during the mean lifetime of an electron) so that the only terms to be derived are the production and loss rates.

The rate of production of electrons p_e is proportional to the loss of ionizing radiation per unit path length $\left(p_e(Z) \propto \left.\frac{dI}{dl}\right|_Z\right)$. Figure 5 depicts the geometry and defines the variables used in the derivation. (As can be seen from fig. 5, the atmosphere is assumed to be spherically symmetric.) To determine p_e, it is assumed that the absorption of ionizing solar radiation in an element of atmospheric path length dl is proportional to the radiation flux I, the atmospheric alkali concentration n_A, and the absorption cross section Q, and thus can be written as

$$dI = -IQn_A dl \tag{8}$$

where the I and Q are wavelength dependent. This wavelength dependence will be accounted for later in this development.

From figure 5

$$i_p = \left(R_p + h\right) \sin \lambda = \left(R_p + Z\right) \sin \chi \tag{9}$$

and

$$l = -i_p \cot \lambda$$

where χ is the solar zenith angle, and $dl = i_p \csc^2 \lambda \, d\lambda$ will be used in equation (8).

In addition to loss of radiation due to ionization, there is a competing reaction from the very weak absorption by CO_2 gas in the 1900 Å to 2100 Å region (absorption coefficient σ). Thus, equation (8) becomes

$$dI = -I\left(Qn_A + \sigma n_{CO_2}\right)dl \tag{10}$$

It is assumed that the diurnal variation in the concentration of the alkali material is very small (in keeping with the long lifetime of the particles), and since their number density is also small, the removal of a source atom must be accounted for in some manner. Therefore, let

$$n_A(h,t) = n_A(h,0) - n_e(Z,t) \tag{11}$$

An initial detailed calculation (integration downward along an ionization path and then stepping ionization paths during the day) showed that $n_e(Z,t)$ follows the n_A height distribution within about 5 percent, so that it will be approximated as

$$n_e(h,t) = G(t) \exp\left(-\frac{h}{6} - 6e^{-h/6}\right) = G(t)\ f(h) \tag{12}$$

Combining equations (10) and (12) yields

$$dI = -I\left\{Q\left[n_A(h,0) - G(t)\ f(h)\right] + \sigma n_{CO_2}\right\} i_p \csc^2 \lambda \, d\lambda \tag{13}$$

From equation (6)

$$dI = -I\left\{Q\ f(h)\left[K - G(t)\right] + \sigma n_{CO_2}\right\} i_p \csc^2 \lambda \, d\lambda \tag{14}$$

so that

$$\int_{I_0}^{I} \frac{dI}{I} = -\int_0^{\chi} \left\{ Q\, f(h)\left[K - G(t)\right] + \sigma n_{CO_2} \right\} i_p \csc^2 \lambda \, d\lambda \tag{15}$$

or

$$I = I_0 \exp\left(-\int_0^{\chi} \left\{ Q\, f(h)\left[K - G(t)\right] + \sigma n_{CO_2} \right\} i_p \csc^2 \lambda \, d\lambda \right) \tag{16}$$

where $h = i_p \csc \lambda - R_p$.

The rate of production of electrons is

$$p_e = -\delta \left. \frac{dI}{dZ} \right|_Z \tag{17}$$

where δ is the number of electrons released per photon absorbed for ionization. Substituting equation (16) into equation (17) then gives

$$p_e = \delta I \left\{ Q\left[n_A(Z,0) - G(t)\, f(Z)\right] \right\} \tag{18}$$

or

$$p_e = \delta I_0 \left\{ Q\left[n_A(Z,0) - G(t)\, f(Z)\right] \right\} \exp\left(-\int_0^{\chi} \left\{ Q\, f(h)\left[K - G(t)\right] + \sigma n_{CO_2} i_p \csc^2 \lambda \right\} d\lambda \right) \tag{19}$$

where $h = i_p \csc \lambda - R_p$.

Since the ionization cross section and the solar flux are both wavelength dependent, the probability of ionization can be written as

$$P = \int_{\lambda_1}^{\lambda_2} Q I_0 \, d\lambda$$

where Q is the absorption cross section and I_0 is the solar flux per unit wavelength. For alkali metals Q varies from about 10^{-22} to 10^{-18} cm^{-2}. (See refs. 67 and 68.) By integrating over the wavelength, P varies between 3×10^{-8} sec^{-1} and 3×10^{-4} sec^{-1}, where $\lambda_1 = 1900$ Å and $\lambda_2 = 2700$ Å, and these values, which are roughly the same as those for Earth (ref. 69), are used for QI_0 in equation (19).

The time-dependent term in the production term is the variable χ (solar zenith angle). The variable χ is related to ϕ (local time measured from noon) by

$$\cos \chi = \sin D \sin (LAT) + \cos D \cos (LAT) \cos \phi \tag{20}$$

where D is the declination of the Sun, LAT is the latitude at point d at height Z and

$$t = \frac{88\,775\phi}{2\pi} = 1.41 \times 10^4\ \phi \tag{21}$$

since there are 88 775 seconds in the Martian solar day.

The conditions for the Sun not to be visible at point d are

$$\left.\begin{aligned} &\cos \chi < 0 \\ &\left|\left(1 + \frac{Z}{R_p}\right) \sin \chi\right| < 1 \end{aligned}\right\} \tag{22}$$

and if these conditions are met

$$p_e \equiv 0 \tag{23}$$

There were two types of loss reactions considered. The first is radiative recombination in which the ionized material recombines directly with an electron. This type of reaction is schematically

$$A + h\nu \rightarrow A^+ + e \qquad \text{(Production)} \tag{24}$$

and

$$A^+ + e \rightarrow A + h\nu \qquad \text{(Radiative recombination)} \tag{25}$$

If the atmosphere is electrically neutral, this reaction has a loss term of

$$L = -\alpha n_e^2 \tag{26}$$

The second type of loss reaction is a more complicated process in the atmosphere, such as

$$A + h\nu \rightarrow A^+ + e \qquad \text{(Production)}$$

followed by the two-step process

$$A^+ + CO_2 + CO_2 \rightarrow A^+CO_2 + CO_2 \qquad \text{(Rate coefficient } K_{27}) \qquad (27)$$

and

$$A^+CO_2 + e^- \rightarrow A + CO_2 \qquad \text{(Rate coefficient } K_{28}) \qquad (28)$$

A second reaction of the same type is the process:

$$A^+ + M \rightarrow A^+M \qquad \text{(Rate coefficient } K_{29}) \qquad (29)$$

$$A^+M + e^- \rightarrow AM \qquad \text{(Rate coefficient } K_{30}) \qquad (30)$$

Reaction pair (eqs. (27) and (28)) is called CO_2 clustering (ref. 67) and reaction pair (eqs. (29) and (30)) would be using a dust particle as a recombination center, such as suggested previously. (See ref. 66.) In both reaction pairs (eqs. (27) and (28)) and (eqs. (29) and (30)), if the rate constants are such that

$$K_{27}(nCO_2)^2 >> K_{28}n_e$$

or

$$K_{29}n_n >> K_{30}n_e$$

then the loss process can again be characterized by equation (26)

$$L = -\alpha n_e^2$$

The value of α varies greatly, depending on whether the loss process is only radiative recombination or some combination of the processes discussed. The range of values used here is from 2×10^{-12} cm^3-sec^{-1} to 10^{-6} cm^3-sec^{-1}. (See refs. 69 to 72.)

Finally, the production and loss terms are combined into the simplified continuity equation to yield

$$\frac{dn_e}{dt} = p_e - L \qquad (31)$$

or combining with equation (21)

$$\frac{dn_e}{d\phi} = (1.41 \times 10^4)(p_e - L) \qquad (32)$$

where p_e is defined by equation (19), L by equation (26), and the relation of χ to ϕ by equation (20).

A computer program was developed to solve equation (32). Inputs to the program are height in the atmosphere, latitude, Sun declination angle, and constants for the production rate, loss rate, and alkali number density. The program starts with zero initial electron density and integrates equation (32) forward in time by using the final electron density of the previous day as the starting condition for the successive day.

The differential equation (32) is integrated by a fifth-order integration subroutine. The classical fourth-order Runge-Kutta formula is applied in conjunction with Richardson's extrapolation to the limit theory. The subroutine is a variable interval size routine in which the interval is varied to meet a specified local relative truncation error. A second subroutine is used to compute the integral in the production function (eq. (19)). The current values of all variables, as updated from the differential equation subroutine, are used in a 10-point Gauss quadrature integration subroutine. The accuracy of these subroutines is far better than is required for the problem at this time, since the accuracy of the parameters characterizing the electron layer are order-of-magnitude estimates.

At the end of three Martian diurnal cycles, the results were printed and compared. If convergence

$$\frac{n_e(t + 1\ \text{day}) - n_e(t)}{n_e(t + 1\ \text{day})} \approx 10^{-3}$$

had occurred, the results were plotted; if not, then the program was continued from the last computing point or new initial conditions were imposed and the program rerun.

APPROXIMATE SOLUTION OF SOME EQUATIONS OF INTEREST

In order to obtain an estimate of the effect that the variation of coefficients (such as the absorption and recombination coefficients) would have on the electron layer and also to reduce the range and time of the computer runs, several approximations to the previously described equations were developed. The first was developed to approximate the maximum electron density. In order to do this, two approximations were made in the electron production term (eq. (19)): (1) the effect of CO_2 absorption was negligible ($\sigma \leqq 10^{-22}$ cm^{-2}) and (2) since the alkali layer has a small number density (characterized by the parameter K) and such a small absorption cross section, the product QK is sufficiently small to drop the exponential time dependence term in equation (19). Since the maximum electron density will occur when $\frac{dn_e}{dt} = 0$ (if reached),

$$I_0\left[Q(n_A - n_{e,max})\right] = \alpha n_{e,max}^2 \tag{33}$$

so that if

$$W \equiv \frac{\int_{\lambda_1}^{\lambda_2} QI_0 \, d\lambda}{\alpha} \tag{34}$$

$$n_{e,max}(Z) = \frac{W}{2}\left[\sqrt{1 + \frac{4n_A(Z)}{W}} - 1\right] \tag{35}$$

From equation (35) (under the same assumptions as eq. (33)) can also be found the required alkali concentration for a given maximum electron density, that is,

$$n_A(Z) = \frac{n_{e,max}^2(Z) + Wn_{e,max}(Z)}{W} \tag{36}$$

The second equation describes the decline in the electron number density after the Sun sets. The differential equation is

$$\frac{dn_e}{dt} = -\alpha n_e^2 \tag{37}$$

the solution of which is

$$n_e(Z,t) = \frac{n_e(Z,t_0)}{1 + \alpha n_e(Z,t_0)(t - t_0)} \tag{38}$$

or rewritten

$$\alpha = \frac{\frac{n_e(Z,t_0)}{n_e(Z,t)} - 1}{n_e(Z,t_0)(t - t_0)} \tag{39}$$

Equations (36) and (39) are used later to narrow the range of acceptable coefficients. The final results to be presented, however, are based on the numerical solutions of equation (32).

RESULTS AND DISCUSSION

All the computer simulations were made for a latitude of 45° and a Sun declination angle of 0° (corresponding to autumnal or vernal equinox). On the basis of published data, the range of the absorption cross section was 10^{-22} to 10^{-18} cm^2 and the range of the recombination coefficients was from 2×10^{-12} to 10^{-6} cm^3-sec^{-1}.

Tables I and II list the coefficients for each model and the electron densities for each model at eight altitudes in the atmosphere. In table I there are two electron densities listed for each model at each altitude. The upper entry is the expected peak equilibrium electron density as obtained from the approximation equation (35). The lower entry is the actual maximum electron density as computed from the time-dependent equations. Again, in table II there are two electron densities listed for each model at each altitude. In table II the upper number corresponds to the expected minimum electron density obtained by using equation (38), and the lower number is the minimum computed electron density as computed from the time-dependent equations. Some general observations can be made from these tables. These observations will be shown in further detail in the figures. The first is that equation (35) gives a reasonable approximation for the peak value of the electron number density and, as is shown in equation (35), the larger the value of W $\left(W = \alpha^{-1} \int QI_0 \, d\lambda\right)$, the larger the peak electron number density. The second observation is that the smaller the value of αn_e, the less the nighttime decay of the electron density as was predicted by equation (38). Included with the discussion of the models is their relative convergence rate. Each model started with an initial electron density of zero electrons per cm^3. The rate of convergence is a probable indicator of the relative stability of the electron layer to atmospheric perturbations.

Figure 6 presents plots of the electron density for model 0. Model 0 has constants of $\alpha = 2 \times 10^{-12}$ cm^3-sec^{-1}, $Q = 10^{-22}$ cm^2, and $K = 9.78 \times 10^5$ cm^{-3}. In figure 6(a) is plotted the variation of electron density with hour angle for eight altitudes in the atmosphere. The hour angle is related to the time of day by equation (20). Examples of local times are $\phi = -90^{\circ}$ is approximately sunrise, $\phi = 0$ is local noon, $\phi = 90^{\circ}$ is approximately local sunset, and $\phi = \pm 180^{\circ}$ is midnight. Figure 6(b) is a plot of the variation of electron density with altitude for the four times just illustrated. (Profiles in fig. 6(b) are coincident.) Model 0 has a large value of W and also has a large peak electron density (2×10^4 cm^{-3}). This model has the smallest value of αn_e; thus, the electron density exhibits an almost imperceptible nighttime decay. The lack of decay is exhibited in figure 6(b), where the profiles for the four times of day all lie on each other. Model 0 was converging so slowly that the computation was restarted by using electron densities slightly lower than the values obtained from equation (35). This procedure, in effect, moves time forward in a large step and results in a convergence of $\Delta n_e/n_e$ between morning terminators of about 10^{-4}.

Model 1 ($\alpha = 2 \times 10^{-12}$ cm^3-sec^{-1}, $Q = 10^{-18}$ cm^2, and $K = 9.78 \times 10^5$) results are plotted in figure 7. The value of W for model 1 is very large and results in the large electron density are shown in figure 7(a). Again, the value of αn_e is small and the variation of electron density is very small; as a result, all four time curves apparently coincide in figure 7(b). Model 1 converged in about a week of Martian time.

Model 2 ($\alpha = 10^{-6}$ cm^3-sec^{-1}, $Q = 10^{-22}$ cm^2, $K = 9.78 \times 10^5$ cm^{-3}) shows a day-night electron density variation of the type needed to explain the diurnal pressure variation. It shows a diurnal equilibrium, that is, the cycle repeats daily, but it does not exhibit an equilibrium in the sense that the time derivative of the electron density equals zero. This effect can be seen in figure 8(a) where there is a large discontinuity in dn_e/dt at the terminators, no equilibrium concentration is reached, and yet diurnal equilibrium is established. Model 2 has a small value of W; this condition is exhibited by the extremely low electron densities achieved (on the order of one five-hundredths of the electron densities of model 0, for example). The value of αn_e is in the midrange of those investigated and results in the slow decay in the density distribution during the night. This effect can be seen in figure 8(b) which is the first model to exhibit diurnal variation of the electron profile. Model 2 was slow to converge and convergence was difficult to determine because of the small numerical value of electron density.

Model 3 ($\alpha = 10^{-6}$ cm^3-sec^{-1}, $Q = 10^{-18}$ cm^2, $K = 9.78 \times 10^5$ cm^{-3}) completes the extremes of Q and α investigated and also exhibits the third type of diurnal variation encountered in the investigation. This diurnal variation is evident in figure 9(a). There is a very sharp rise in electron density at sunrise (which is a result of the large value of Q); an equilibrium of $dn_e/dt = 0$ is reached during the sunlight hours; and then there is a very sharp decay in the electron density at night (which is a result of the large value of αn_e). From figure 9(b), the profile plot for model 3, it can be seen that for the midrange value of W, the peak electron density is not too large, but the large diurnal variation in electron density, which is required to explain the pressure differences, is present. Model 3 reached equilibrium in about 6 days of Martian time.

To complete this preliminary analysis, the midrange values of $Q = 10^{-22}$ cm^2 and $\alpha = 10^{-8}$ cm^3-sec^{-1} were investigated. Model 6 ($\alpha = 10^{-8}$ cm^3-sec^{-1}, $Q = 10^{-22}$ cm^2, $K = 9.78 \times 10^5$ cm^{-3}) results are plotted in figure 10. The value of W is small and, as a result, the electron number density is low, as can be seen in figure 10(a). The value αn_e was also small and implies slow decay; this effect is exhibited in figure 10. Model 6 reached equilibrium after about 30 diurnal cycles.

The results of model 7 ($\alpha = 10^{-8}$ cm^3-sec^{-1}, $Q = 10^{-18}$ cm^2, $K = 9.78 \times 10^5$ cm^3) are plotted in figure 11. The recombination coefficient α is such that αn_e is large and thus the distribution should exhibit a pronounced nighttime decay. This decay can be seen in figure 11(a). The value of W for model 7 is also large and therefore the peak electron number density is large. (See fig. 11(b).)

A MODEL CONSISTENT WITH OBSERVED DIURNAL PRESSURE VARIATIONS

Examination of the foregoing results indicates that the sinusoidal diurnal variation of the electron density which is observed in the Earth's ionosphere is not duplicated by this low-lying electron layer on Mars. This effect is predominately due to the product of the absorption cross section and the source number density. When this product is small, the exponential term in the electron production (eq. (35)), which accounts for the time variation, is very weak. Therefore, even for the long slant paths at the terminators, the ionizing radiation on Mars has only been slightly attenuated. In fact, the production function, for the low-lying electron, can be thought of almost as a light switch having two positions – on and off.

The second result of this study came after the conclusion of all the actual time-dependent calculations. The result was that equation (35), which neglected time dependence, gave a good approximation to the peak electron number density (6 percent average error). Thus, as more and better data about the Martian atmosphere become available, equation (35) can be used to give a quick approximation as to the effect of the low-lying electron layer on the atmospheric properties deduced by radio occultation and vice versa.

The third result was that the larger the value of αn_e, the faster the nighttime decay of the electron density. This result would be expected from an examination of equation (38). The general trend was that for values of $\alpha n_e < 10^{-6}$ sec^{-1}, the distribution showed no diurnal variation; for values 10^{-4} sec$^{-1} > \alpha n_e > 10^{-6}$ sec^{-1}, the distribution exhibited a sawtooth variation; and for $\alpha n_e > 10^{-4}$ sec^{-1}, the distribution showed a sharp rise and fall or a square wave.

Combining the results of the foregoing study with the measured pressure data should allow the possible range of the various coefficients to be narrowed. From the discussion of pressure data, it is clear that the peak electron density must be on the order of 6×10^4 electrons per cm^3 and that this number must decrease at night to the point of being undetectable. To determine the recombination coefficient the following equation is used:

$$\alpha = \frac{\dfrac{n_e(Z,t_0)}{n_e(Z,t)} - 1}{n_e(Z,t_0)(t - t_0)}$$

with n_e (10.75 km, sunset) $\approx 6 \times 10^4$ cm^{-3}, (t - t_0(sunset)) $\approx$ 2 hours, and n_e (10.75 km, t) $\approx 6 \times 10^3$ cm^{-3}, which is an electron density low enough to be masked by an experiment error of 4 percent at the pressure levels in question. For these values, the resulting recombination coefficient must be on the order of 2×10^{-8} cm^3-sec^{-1}; for ease of calculation, let $\alpha = 10^{-8}$ cm^3-sec^{-1}. Then, to determine the required alkali source number density, equation (36) is rewritten with $n_A(Z) = K\,f(Z)$

$$K = \frac{n_{e,max}^2(Z) + W\,n_{e,max}(Z)}{W\,f(Z)}$$

where $f(Z) = \exp\left[-\left(\frac{Z}{6} + 6e^{-Z/6}\right)\right]$ and $W = \alpha^{-1}\int QI_0\,d\lambda$. Therefore by assuming $Q = 10^{-18}$ cm^2, K is of the order of 2.92×10^6 cm^{-3}, and means a peak density of alkali atoms of 1.79×10^5 cm^{-3}. Having a 0.2-micrometer particle sublimate one ten-thousandths of its mass in alkali atoms would require a dust distribution of only 9 particles per cm^3 in order to produce the required alkali atom density. One outcome of this study, then, is that the coefficients of $\alpha = 10^{-8}$ cm^3-sec^{-1}, $Q = 10^{-18}$ cm^2, and $K = 2.92 \times 10^6$ cm^{-3}, which are within the range of laboratory measurements of the processes involved, should produce an electron density model which will explain the apparent diurnal pressure variation. These coefficients are used in model 8, and the computed electron densities are plotted in figure 12. The effect of the larger cross section can be seen in figure 12(a) as the extremely rapid rise in the electron density immediately after sunrise. The electron density reaches an equilibrium of about 6×10^4 electrons per cm^3, as required, for the entire daylight period. The medium large product of αn_e produces a rapid nighttime decay as is shown in figure 12. From figure 12(b) can be seen the electron density height profiles for four different times in the Martian day. The morning profile has already nearly 90 percent of the equilibrium density shortly after sunrise. The noon and evening profiles coincide at the equilibrium densities. Finally, the extremely rapid decay can be seen as the midnight profile has fallen to 7 percent of the equilibrium density.

CONCLUSIONS

There are some general conclusions about the low-lying electron layer distribution that can be inferred from this study.

(1) Because the product of the absorption cross section and the number density of the ionized constituent is small, the production term in the continuity equation has very little time dependence during the day. Therefore, the sinusoidal time variation in electron density that is observed on Earth is not present in the low-altitude electron distribution on Mars.

(2) The value of αn_e determines the shape of the curves of electron density as a function of time; thus, for electron layers that are of possible importance in the explanation of the radio occultation pressure discrepancies, the value of αn_e (where α is the recombination coefficient and n_e is the electron density) must be at least equal to or greater than about 10^{-4} sec^{-1}.

(3) For $\alpha n_e \geqq 10^{-4}$ sec^{-1}, a good approximation to the peak electron density daytime distribution is obtained.

From the preliminary Martian radio occultation data, it has been found that the following values for the coefficients used in this study would adequately account for an observed 1-mb difference between day and night surface pressures: $\alpha = 10^{-8}$ cm^3-sec^{-1}, $Q = 10^{-18}$ cm^2, and $K = 2.92 \times 10^6$ cm^{-3} (Q is ionization absorption cross section and K is an alkali scaling number). This value of the absorption coefficient is in the range of that measured for the alkali metals. The value of the recombination coefficient ($\approx 10^{-8}$ cm^3-sec^{-1}) implies that radiative recombination is not the dominant process for the loss of electrons. The loss mechanism wherein the dust acts as a recombination site is also not very probable since the dust density is numerically so small. Thus, the most probable mechanism for the loss of electrons is CO_2 clustering to the alkali ion, which has a very high rate coefficient.

A low-altitude residual dust layer in the Martian atmosphere has been observed and measured and is theoretically required to explain temperature lapse rates; this dust layer is composed of alkali and alkali compounds having low ionization potentials; and the Martian atmosphere has low concentrations of O, O_2, and O_3 that allow solar ultraviolet radiation to penetrate to the planet's surface. From a consideration of these factors, it is concluded that there is a low-altitude electron layer. This study has shown that it is well within the range of possible conditions in the atmosphere to obtain peak electron densities on the order of 6×10^4 electrons/cm^3, which would be required to explain the observed diurnal pressure differences.

Several areas of research utilizing currently available data could be undertaken at the present time. The first is a comprehensive reanalysis of present Martian atmospheric pressure data to determine whether the effects of the low-altitude electron layer are of sufficient magnitude to be able to define more closely the physical properties of the layer. Secondly, studies can be initiated toward a simple analysis of meteoric ablation. These studies would give an idea as to how closely an equilibrium distribution of ablated particles matches the required aerosol concentration layer. Differences between the two, if any, would give a starting point as to the amount of aerosols that must be lifted into the Martian atmosphere by meteorological phenomena.

It is proposed that an experiment be designed to search for and examine this low-altitude electron layer. The discovery and understanding of such a layer would not only be useful in the study of the Martian atmosphere but would also aid in the modeling of the poorly understood Earth's alkali metal ion region and sporadic E layer, since the Martian analysis would be much simpler (because of the much simpler Mars atmosphere). For example, several models of the Earth's alkali layer involve wind-induced $\vec{V} \times \vec{B}$ shear layers of charged dust particles as a source of alkali atoms or involve wind-induced $\vec{V} \times \vec{B}$ layers as a removal mechanism for the alkali ion ($\vec{V}$ is atmospheric wind velocity and $\vec{B}$ is planetary magnetic field). Thus, on Mars where the magnetic field is less than 10^{-3} times that of the Earth, the analysis of the effects of the lack of large magnitude $\vec{V} \times \vec{B}$ forces in the alkali layer formation would have direct bearing on Earth models requiring such forces.

Two experiments which could be utilized to detect the low-altitude electron layer are a two-frequency radio occultation experiment or a twilight glow experiment. The two-frequency radio occultation experiment (currently planned for the Viking orbiter) will yield two values for the index of refraction of the Martian atmosphere because of the different probing frequencies. The subtraction of the two indices of refraction and the knowledge of the frequencies will yield a close approximation to the electron number density (since the index of refraction of most low-density neutral gases is not very wavelength dependent). The twilight glow experiment would be to search for emission lines in the atmospheric twilight. The identification of lines allows the delineation of the alkali species and the intensity of the line can be related to the species number density. Such an experiment could be implemented on an orbiting spacecraft and could be combined with some similar type of emission experiment.

Langley Research Center,
National Aeronautics and Space Administration,
Hampton, Va., August 1, 1974.

APPENDIX

DERIVATION OF COMPOSITE INDEX OF REFRACTION AND REFRACTIVITY

This appendix is a short derivation of the steps needed to determine equations (1) and (3). To derive equation (1), it is assumed at first that in an electrically neutral, nonconducting (no free electrons) atmosphere of dielectric constant ϵ_n, one of Maxwell's equations can be written as

$$\nabla \times \vec{H} = \epsilon_n \frac{\partial \vec{E}}{\partial t} \tag{A1}$$

If now the electrically neutral medium contains free electrons (density n_e) in addition to the neutral part of the medium, then the conducting part of the medium can be characterized by a conductivity σ and Maxwell's equation is supplemented by Ohm's law

$$\vec{J} = \sigma\vec{E} = n_e(e^-)\vec{v} \tag{A2}$$

where $\vec{v}$ is the velocity of electron so that

$$\nabla \times \vec{H} = \epsilon_n \frac{\partial \vec{E}}{\partial t} + \vec{J} \tag{A3}$$

or

$$\nabla \times \vec{H} = \epsilon_n \frac{\partial \vec{E}}{\partial t} + \sigma\vec{E} \tag{A4}$$

If it is assumed that the right-hand side of equation (A4) can be expressed as some composite dielectric coefficient times $\frac{\partial \vec{E}}{\partial t}$ to reduce the equation to the simple form of equation (A1), then

$$\nabla \times \vec{H} = \epsilon_n \frac{\partial \vec{E}}{\partial t} + \sigma\vec{E} = \epsilon_c \frac{\partial \vec{E}}{\partial t} \tag{A5}$$

To determine the conductivity, assume that there are negligible collisions so that the equation of motion of an electron is

$$m \frac{d\vec{v}}{dt} = e^-\vec{E} \tag{A6}$$

If

$$\vec{E} = E_0 e^{-i\omega t} \tag{A7}$$

then

$$\vec{v} = \frac{ie^-}{\omega m} \vec{E} \tag{A8}$$

From equation (A2)

$$\sigma\vec{E} = n_e e^- \vec{v} = \frac{in_e(e^-)^2}{\omega m} \vec{E} \tag{A9}$$

so that

$$\sigma = \frac{in_e(e^-)^2}{\omega m} \tag{A10}$$

Substituting equation (A10) into equation (A5) yields

$$\epsilon_n \frac{\partial\vec{E}}{\partial t} + \frac{in_e(e^-)^2}{\omega m} \vec{E} = \epsilon_c \frac{\partial\vec{E}}{\partial t} \tag{A11}$$

or

$$-i\omega\epsilon_n + \frac{in_e(e^-)^2}{\omega m} = -i\omega\epsilon_c \tag{A12}$$

or rearranged

$$\epsilon_c = \epsilon_n - \frac{n_e(e^-)^2}{\omega^2 m} = \epsilon_n - \frac{n_e}{m}\left(\frac{e^-}{2\pi f}\right)^2 \tag{A13}$$

If the magnetic field is small so that the magnetic permeability of the medium is approximately that of free space, then $\mu \equiv \sqrt{\frac{\epsilon}{\epsilon_0}}$ is the real index of refraction and

$$\mu_c^2 = \mu_n^2 - \frac{n_e(e^-)^2}{(2\pi)^2 \epsilon_0 m f^2} \tag{A14}$$

which is equation (1).

To determine equation (3), define

$$X \equiv \frac{n_e(e^-)^2}{(2\pi)^2 \epsilon_0 m f^2} \tag{A15}$$

then, equation (A14) becomes

$$\mu_c{}^2 = \mu_n{}^2 - X \tag{A16}$$

The index of refraction of just the electrons is

$$\mu_e{}^2 = (1 + N_e \times 10^{-6})^2 = 1 - X \tag{A17}$$

so that

$$1 + N_e \times 10^{-6} = \sqrt{1 - X} \approx 1 - \frac{1}{2} X \tag{A18}$$

or

$$N_e \times 10^{-6} \approx -\frac{1}{2} X \tag{A19}$$

Substituting equation (A16) into equation (A19) yields

$$N_e \times 10^{-6} \approx \frac{1}{2}(\mu_c{}^2 - \mu_n{}^2) = \frac{1}{2}(\mu_c - \mu_n)(\mu_c + \mu_n) \tag{A20}$$

Now

$$\mu_c + \mu_n \approx 2 \tag{A21}$$

and

$$\mu \equiv 1 + N \times 10^{-6} \tag{A22}$$

so that equation (A20) becomes

$$N_e \times 10^{-6} \approx \frac{1}{2}(1 + N_c \times 10^{-6} - 1 - N_n \times 10^{-6})(2) \tag{A23}$$

$$N_e \approx N_c - N_n \tag{A24}$$

which is equation (3).

REFERENCES

1. Leighton, R. B.; Horowitz, N. H.; et al.: Television Observations From Mariners 6 and 7. Mariner-Mars 1969, NASA SP-225, 1969, pp. 37-82.
2. Masursky, Harold; Batson, R. M.; et al.: Mariner 9 Television Reconnaissance of Mars and Its Satellites: Preliminary Results. Science, vol. 175, no. 4019, Jan. 1972, pp. 294-305.
3. Leovy, C. B.; Briggs, G. A.; et al.: The Martian Atmosphere: Mariner 9 Television Experiment Progress Report. ICARUS, vol. 17, 1972, pp. 373-393.
4. Herr, K. C.; and Pimentel, G. C.: Infrared Spectroscopy Mariner-Mars 1969. NASA SP-225, 1969, pp. 83-96.
5. Hanel, R. A.; Conrath, B. J.; et al.: Infrared Spectroscopy Experiment on the Mariner 9 Mission: Preliminary Results. Science, vol. 175, no. 4019, Jan. 1972, pp. 305-308.
6. Hanel, R.; Conrath, B.; et al.: Investigation of the Martian Environment by Infrared Spectroscopy on Mariner 9. ICARUS, vol. 17, no. 2, Oct. 1972, pp. 423-442.
7. Neugebauer, G.; Münch, G.; et al.: Infrared Radiometry. Mariner-Mars 1969. NASA SP-225, 1969, pp. 105-109.
8. Chase, S. C., Jr.; Hatzenbeler, H.; et al.: Infrared Radiometry Experiment on Mariner 9. Science, vol. 175, no. 4019, Jan. 1972, pp. 308-309.
9. Barth, C. A.; Stewart, A. I.; et al.: Mariner 9 Ultraviolet Spectrometer Experiment: Mars Airglow Spectroscopy and Variations in Lyman Alpha. ICARUS, vol. 17, no. 2, Oct. 1972, pp. 457-468.
10. Barth, Charles A.; Hord, Charles W.; et al.: Mariner 9 Ultraviolet Spectrometer Experiment: Initial Results. Science, vol. 175, no. 4019, Jan. 1972, pp. 309-312.
11. Barth, C. A.; Fastie, W. G.; et al.: Ultraviolet Spectroscopy. Mariner-Mars 1969, NASA SP-225, 1969, pp. 97-104.
12. Stewart, A. I.; Barth, C. A.; et al.: Mariner 9 Ultraviolet Spectrometer Experiment: Structure of Mars' Upper Atmosphere. ICARUS, vol. 17, no. 2, Oct. 1972, pp. 469-474.
13. Fjeldbo, Gunnar; and Eshleman, Von R.: The Atmosphere of Mars Analyzed by Integral Inversion of the Mariner IV Occultation Data. Planet. Space Sci., vol. 16, no. 8, Aug. 1968, pp. 1035-1059.

14. Rasool, S. I.; Hogan, J. S.; et al.: Temperature Distributions in the Lower Atmosphere of Mars From Mariner 6 and 7 Radio Occultation Data. J. Atmospheric Sci., vol. 27, no. 5, Aug. 1970, pp. 841-843.

15. Rasool, S. I.; and Stewart, R. W.: Results and Interpretation of the S-Band Occultation Experiments on Mars and Venus. J. Atmospheric Sci., vol. 28, no. 6, Sept. 1971, pp. 869-878.

16. Kliore, A. J.; Cain, D. L.; et al.: Mariner 9 S-Band Martian Occultation Experiment: Initial Results on the Atmosphere and Topography of Mars. Science, vol. 175, no. 4019, Jan. 1972, pp. 313-317.

17. Kliore, Arvydas J.; Cain, Dan L.; et al.: The Atmosphere of Mars From Mariner 9 Radio Occultation Measurements. ICARUS, vol. 17, no. 2, Oct. 1972, pp. 484-516.

18. Hogan, Joseph S.; Stewart, Richard W.; Rasool, S. I.; and Russell, L. H.: Results of the Mariner 6 and 7 Mars Occultation Experiments. NASA TN D-6683, 1972.

19. Kliore, A. J.; Fjeldbo, G.; et al.: S Band Radio Occultation Measurements of the Atmosphere and Topography of Mars With Mariner 9: Extended Mission Coverage of Polar and Intermediate Latitudes. J. Geophys. Res., vol. 78, no. 20, July 1973, pp. 4331-4351.

20. Harrington, J. V.; Grossi, M. D.; and Langworthy, B. M.: Mars Mariner 4 Radio Occultation Experiment: Comments on the Uniqueness of the Results. J. Geophys. Res., vol. 73, no. 9, May 1968, pp. 3039-3041.

21. Michael, William H., Jr.; Wallio, H. Andrew; and Levine, Joel S.: Mars Lower Atmosphere: Some New Implications. Paper presented at XV Plenary Meeting COSPAR (Madrid, Spain), May 1972.

22. Jeffreys, Harold: The Earth. Fourth ed., Cambridge Univ. Press, 1959.

23. Lorell, J.; Born, G. H.; et al.: Gravity Field of Mars From Mariner 9 Tracking Data. Trans. Amer. Geophys. Union, vol. 53, no. 4, Apr. 1972, p. 432.

24. Lorell, J.; Born, G. H.; et al.: Mariner 9 Celestial Mechanics Experiment: Gravity Field and Pole Direction of Mars. Science, vol. 175, no. 4019, Jan. 21, 1972, pp. 317-320.

25. Runcorn, S. K.: On the Implications of the Shape of Mars. ICARUS, vol. 18, no. 1, Jan. 1973, pp. 109-112.

26. Schubert, G.; and Lingenfelter, R. E.: Martian Centre of Mass – Centre of Figure Offset. Nature, vol. 242, no. 5395, Mar. 1973, pp. 251-252.

27. Belton, Michael J. S.; and Hunten, Donald M.: The Distribution of CO_2 on Mars: A Spectroscopic Determination of Surface Topography. ICARUS, vol. 15, 1971, pp. 204-232.

28. McElroy, Michael B.: Structure of the Venus and Mars Atmospheres. J. Geophys. Res., vol. 74, no. 1, Jan. 1969, pp. 29-41.

29. Cloutier, P. A.; McElroy, M. B.; and Michel, F. C.: Modification of the Martian Ionosphere by the Solar Wind. J. Geophys. Res., vol. 74, no. 26, Dec. 1969, pp. 6215-6228.

30. Stewart, Richard W.: The Electron Distributions in the Mars and Venus Upper Atmospheres. J. Atmos. Sci., vol. 28, no. 6, Sept. 1971, pp. 1069-1073.

31. Gringauz, K. I.; and Breus, T. K.: Comparative Characteristics of the Ionospheres of the Planets of the Terrestrial Group: Mars, Venus, and the Earth. Space Science Reviews, vol. 10, no. 6, C. de Jager, ed., D. Reidel Publ. Co., June 1970, pp. 743-769.

32. Kolosov, M. A.; Yakovlev, O. I.; et al.: Preliminary Results of Martian-Atmosphere Research With the Mars-2 Satellite. Soviet Physics Doklady, vol. 17, no. 10, Apr. 1973, pp. 949-950.

33. Whitten, R. C.; Poppoff, I. G.; and Sims, J. S.: The Ionosphere of Mars Below 80 km Altitude. I – Quiescent Conditions. Planet. Space Sci., vol. 19, no. 2, Feb. 1971, pp. 243-250.

34. Whitten, R. C.; Poppoff, I. G.; et al.: The Ionosphere of Mars Below 80 km Altitude. II – Solar Cosmic Ray Event. Planet. Space Sci., vol. 19, no. 8, Aug. 1971, pp. 971-979.

35. Koval, I. K.: The Martian "Peak." Priroda, no. 4, 1972, pp. 2-9.

36. Herzberg, Gerhard: Molecular Spectra and Molecular Structure. III – Electronic Spectra and Electronic Structure of Polyatomic Molecules. D. Van Nostrand Co., Inc., c.1966.

37. Visconti, G.: Enhancement of Upper Atmospheric Sodium From Sporadic Dust Influxes. J. Atmospheric and Terrestrial Phys., vol. 35, no. 7, July 1973, pp. 1331-1340.

38. Koval, I. K.: Atmosphere and Surface of Mars. Solar System Res., vol. 5, no. 3, July-Sept. 1971.

39. Hanel, R.; Conrath, B.; et al.: Investigation of the Martian Environment by Infrared Spectroscopy on Mariner 9. NASA TM X-65993, 1972.

40. Watts, Raymond N., Jr.: Some Mariner 9 Observations of Mars. Sky Telescope, vol. 43, no. 4, Apr. 1972, pp. 208-213.

41. Moroz, V. I.; Ksanfomaliti, L. V.; Kasatkin, A. M.; and Nadzhip, A. E.: Dust Storms on Mars According to Photometric Observations Taken on Board the Mars-3 Automatic Interplanetary Station. NASA TT F-14,818, 1973.

42. Moroz, V. I.: The Mars 2 and Mars 3 Orbital Spacecraft: Results of Studies of the Surface and Atmosphere of Mars. NASA TT F-14,908, 1973.

43. Leovy, Conway B.; Smith, Bradford A.; et al.: Mariner Mars 1969: Atmospheric Results. J. Geophys. Res., vol. 76, no. 2, Jan. 1971, pp. 297-312.

44. Gierasch, Peter J.; and Goody, Richard M.: The Effect of Dust on the Temperature of the Martian Atmosphere. J. Atmospheric Sci., vol. 29, no. 2, Mar. 1972, pp. 400-402.

45. Whitten, R. C.; and Sims, J. S.: The Photolytic Stability of the Martian Atmosphere. Planet. Space Sci., vol. 21, no. 8, Aug. 1973, pp. 1333-1338.

46. Moroz, V. I.; and Ksanfomaliti, L. V.: Preliminary Results of the Astrophysical Observations of Mars From AIS Mars-3. Paper presented at COSPAR 15th Plenary Meeting (Madrid, Spain), May 1972.

47. Smith, Robert E., ed.: Space and Planetary Environment Criteria Guidelines for Use in Space Vehicle Development (1971 Revision). NASA TM X-64627, 1971.

48. Borodin, L. S.: Alkaline Rocks – Indicators of the Earth's Interior. NASA TT F-13,782, 1972.

49. Gierasch, Peter; and Goody, Richard: A Study of the Thermal and Dynamical Structure of the Martian Lower Atmosphere. Planet. Space Sci., vol. 16, no. 5, May 1968, pp. 615-646.

50. Gierasch, Peter; and Sagan, Carl: A Preliminary Assessment of Martian Wind Regimes. ICARUS, vol. 14, no. 3, June 1971, pp. 312-318.

51. Leovy, C. B.; Briggs, G. A.; et al.: The Martian Atmosphere: Mariner 9 Television Experiment Progress Report. ICARUS, vol. 17, no. 2, Oct. 1972, pp. 373-393.

52. Gierasch, P. J.; and Goody, R. M.: A Model of a Martian Great Dust Storm. J. Atmospheric Sci., vol. 30, no. 2, Mar. 1973, pp. 169-179.

53. Gadsden, M.: Sodium in the Upper Atmosphere: Meteoric Origin. J. Atmospheric and Terrestrial Phys., vol. 30, no. 1, Jan. 1968, pp. 151-161.

54. Elterman, Louis; Toolin, Robert B.; and Essex, John D.: Stratospheric Aerosol Measurements With Implications for Global Climate. Appl. Optics, vol. 12, no. 2, Feb. 1973, pp. 330-337.

55. Cox, S. K.; Vonder Haar, T. H.; et al.: Measurements of Absorbed Shortwave Energy in a Tropical Atmosphere. Solar Energy, vol. 14, no. 2, Jan. 1973, pp. 169-173.

56. Cunnold, D. M.; Gray, C. R.; and Merritt, D. C.: Stratospheric Aerosol Layer Detection. J. Geophys. Res., vol. 78, no. 6, Feb. 1973, pp. 920-931.

57. Graham, D. A.; Ichikawa, T.; and Kim, J. S.: Observations of Sodium, Lithium and Potassium Twilightglow at Moscow, Idaho, U.S.A. Ann. Geophys., vol. 27, no. 4, 1971, pp. 483-491.

58. Hanson, W. B.; and Donaldson, J. S.: Sodium Distribution in the Upper Atmosphere. J. Geophys. Res., vol. 72, no. 21, Nov. 1967, pp. 5513-5514.

59. Gadsden, M.: Comparison of Radio-Meteor Rate With Abundance of Sodium in the Upper Atmosphere. Ann. Geophys., vol. 27, no. 3, 1971, pp. 401-406.

60. Istomin, V. G.: Magnesium and Calcium Ions in the Earth's Upper Atmosphere. NASA TT F-69, 1961.

61. Donahue, T. M.; and Meier, R. R.: Distribution of Sodium in the Daytime Upper Atmosphere as Measured by a Rocket Experiment. J. Geophys. Res., vol. 72, no. 11, June 1967, pp. 2803-2829.

62. Hunten, D. M.; and Wallace, L.: Rocket Measurements of the Sodium Dayglow. J. Geophys. Res., vol. 72, no. 1, Jan. 1967, pp. 69-79.

63. Hunten, Donald M.: Spectroscopic Studies of the Twilight Airglow. Space Science Reviews, vol. VI, no. 4, C. de Jager, ed., D. Reidel Publ. Co., Feb. 1967, pp. 493-573.

64. Gadsden, M.: Metallic Atoms and Ions in the Upper Atmosphere. Ann. Geophys., vol. 26, no. 1, 1970, pp. 141-150.

65. Keller, G. E.; and Beyer, R. A.: CO_2 and O_2 Clustering to Sodium Ions. J. Geophys. Res., vol. 76, no. 1, Jan. 1971, pp. 289-290.

66. Zikmunda, J.; and Mohnen, V. A.: Ion Annihilation by Aerosol Particles From Ground Level to 60 km Height. Meteorol. Rdsch., vol. 25, no. 1, 1972, pp. 10-14.

67. Ditchburn, R. W.; Jutsum, P. J.; and Marr, G. V.: The Continuous Absorption of Light in Alkali-Metal Vapours. Proc. Roy. Soc. London, ser. A, vol. 219, no. 1136, Oct. 1953, pp. 89-101.

68. Samson, James A. R.: The Measurement of the Photoionization Cross Sections of the Atomic Gases. Vol. 2, Advances in Atomic and Molecular Physics, D. R. Bates and Immanuel Estermann, eds., Academic Press, Inc., 1966, pp. 177-261.

69. Marmo, F. F.; Pressman, J.; and Aschenbrand, L. M.: Artificial Electron Clouds. II – General Considerations. Planet. Space Sci., vol. 1, no. 4, Sept. 1959, pp. 291-305.

70. Yadava, V. K.; Prasad, R. Y.; and Tolpadi, S. K.: Magnesium and Associated Ionospheric Processes in E_s-Layer Formation. Ann. Geophys., vol. 28, no. 3, 1972, pp. 575-579.

71. Aikin, A. C.; and Goldberg, R. A.: Metallic Ions in the Equatorial Ionosphere. J. Geophys. Res., vol. 78, no. 4, Feb. 1973, pp. 734-745.

72. Narcisi, R. S.: Processes Associated With Metal-Ion Layers in the E Region of the Ionosphere. COSPAR Space Research VIII, A. P. Mitra, L. G. Jacchia, and W. S. Newman, eds., North-Holland Pub. Co. (Holland), 1968, pp. 360-369.

73. Kumer, J. B.: A Spectrum of New Experiments To Investigate Alkali Metal Chemistry in the E Region. RADC-TR-71-293, U.S. Air Force, June 1971. (Available from DDC as AD 737 103.)

TABLE I.- PREDICTED MAXIMUM ELECTRON DENSITIES (UPPER ENTRY) AND COMPUTED MAXIMUM ELECTRON DENSITIES (LOWER ENTRY) FOR EIGHT ALTITUDES IN THE MODEL ATMOSPHERES

Model	Q, cm^2	α, cm^3-sec^{-1}	K, cm^{-3}	W, cm^{-3}	Values of n_e, cm^{-3}, for an altitude, km, of –							
					0	5	10.75	15	20	30	40	50
0	E - 22	2E - 12	9.78E + 05	1.51E + 04	2126 2013	15 491 14 043	23 502 20 770	20 719 18 479	14 427 13 085	4 804 4 540	1148 1090	231 219
1	E - 18	2E - 12		1.51E + 08	2424 2424	31 323 31 323	59 940 59 940	49 041 49 041	28 161 28 161	6 328 6 328	1235 1235	234 234
2	E - 22	E - 06		3.03E - 02	8 6	30 29	42 41	38 37	29 27	13 12	6 4	2 1
3	E - 18	E - 06		3.03E + 02	718 718	2 933 2 932	4 113 4 113	3 706 3 706	2 773 2 773	1 241 1 241	478 478	155 155
6	E - 22	E - 08		3.03	64 62	306 232	424 330	384 298	290 224	136 105	59 48	25 22
7	E - 18	E - 08		3.03E + 04	2256 2256	19 184 19 182	30 087 30 085	26 274 26 273	17 758 17 758	5 375 5 375	1188 1188	232 232
8	E - 18	E - 08	2.92E + 04	3.03E + 04	6035 6035	40 202 40 197	60 044 60 040	53 169 53 167	37 553 37 552	13 170 13 170	3323 3323	685 685

TABLE II.- PREDICTED MINIMUM MORNING ELECTRON DENSITIES (UPPER ENTRY) AND COMPUTED MINIMUM MORNING ELECTRON DENSITIES (LOWER ENTRY) FOR EIGHT ALTITUDES IN THE MODEL ATMOSPHERES

Model	Q, cm^2	α, cm^3-sec^{-1}	K, cm^{-3}	αn_e, sec^{-1}	Values of n_e, cm^{-3}, for an altitude, km, of –							
					0	5	10.75	15	20	30	40	50
0	E - 22	2E - 12	9.78E + 05	4.7E - 08	2125	15 470	23 454	20 684	14 410	4802	1148	231
					2013	14 027	20 735	18 451	13 071	4539	1090	219
1	E - 18	2E - 12		1.2E - 07	2424	31 241	59 646	48 846	28 097	6325	1234	233
					2423	31 241	59 646	48 847	28 097	6324	1235	234
2	E - 22	E - 06		4.2E - 05	6	17	15	15	13	9	4	1
					5	13	15	14	13	8	4	1
3	E - 18	E - 06		4.1E - 03	22	24	24	24	24	25	24	22
					21	23	24	24	24	25	24	22
6	E - 22	E - 08		4.2E - 06	81	27	361	331	260	130	58	24
					60	21	291	266	206	131	47	22
7	E - 18	E - 08		3.0E - 04	1128	2 111	2 248	2 253	2 192	1735	817	213
					1128	2 111	2 248	2 229	2 192	1736	817	214
8	E - 18	E - 08	2.92E + 06	6.0E - 04	1642	2 240	2 335	2 355	2 344	2145	1464	545
					1642	2 239	2 335	2 355	2 344	2145	1464	545

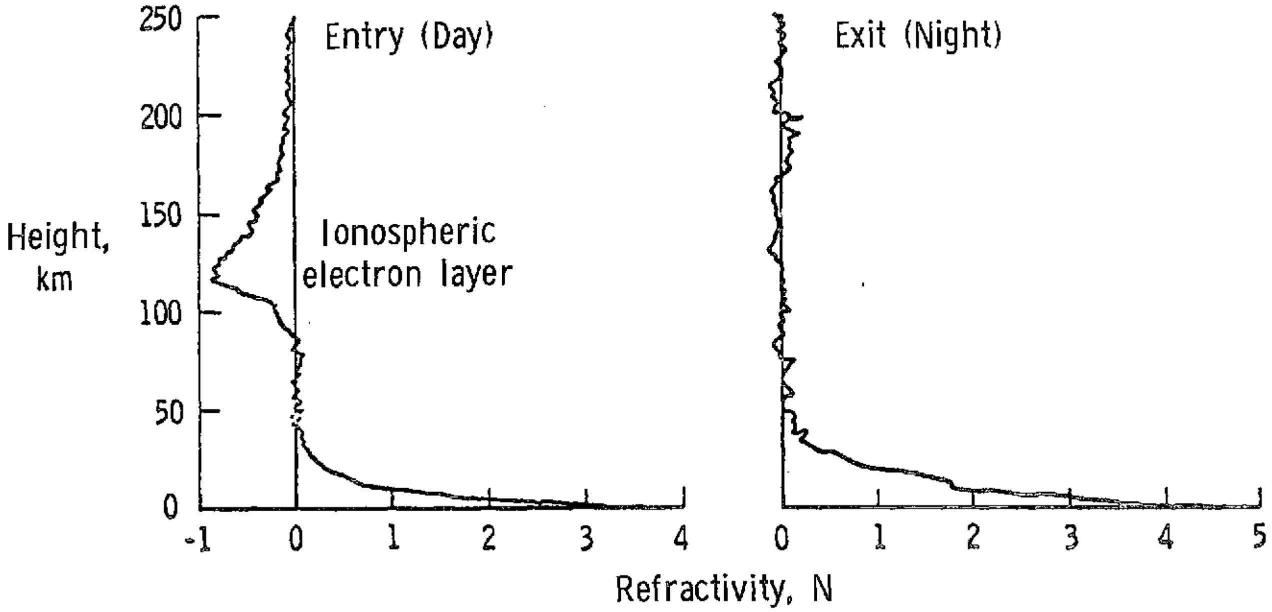

Figure 1.- Sketch of typical atmospheric refractivity profiles for Mars.

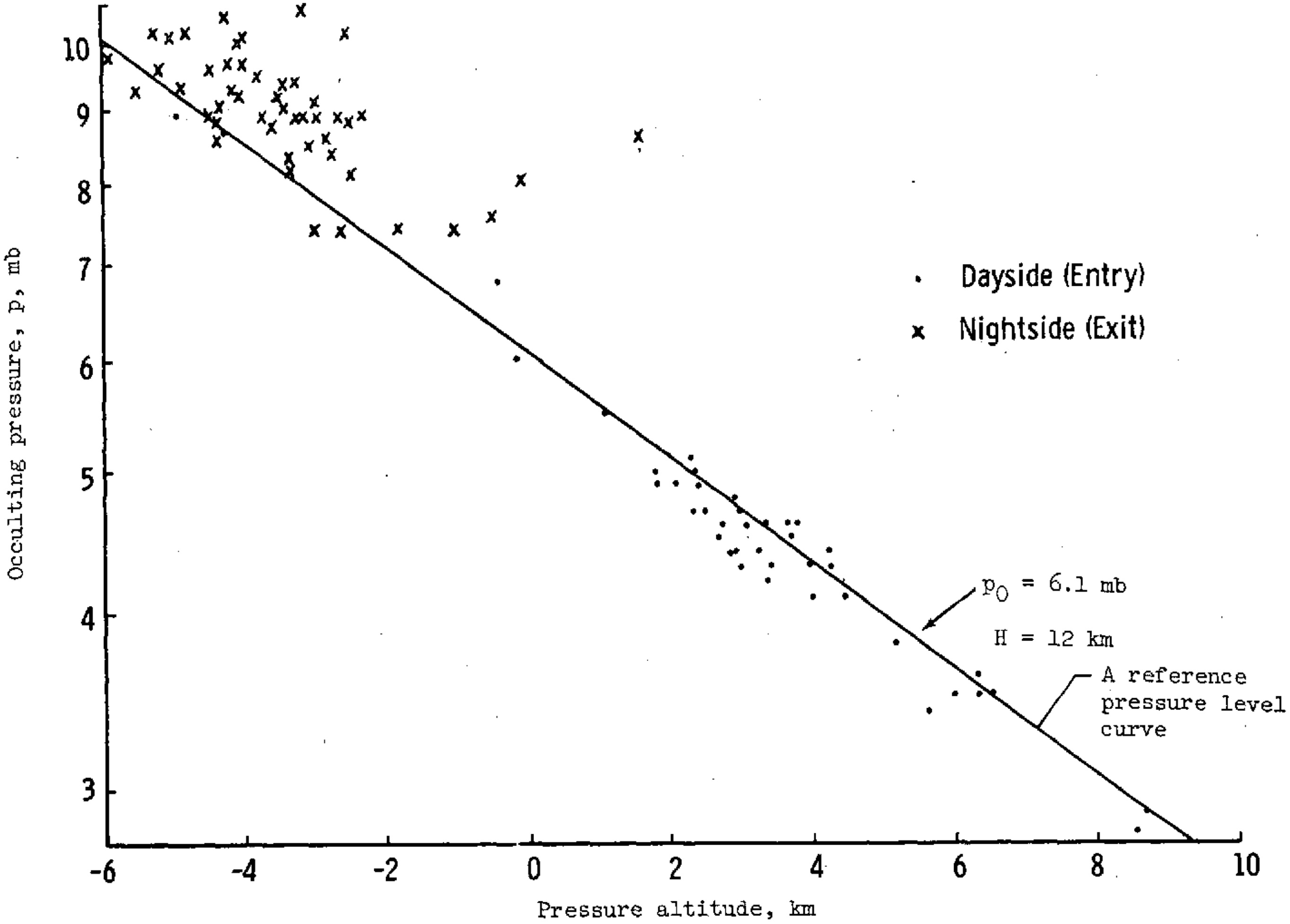

Figure 2.- Dayside and nightside surface pressures plotted against pressure altitude.

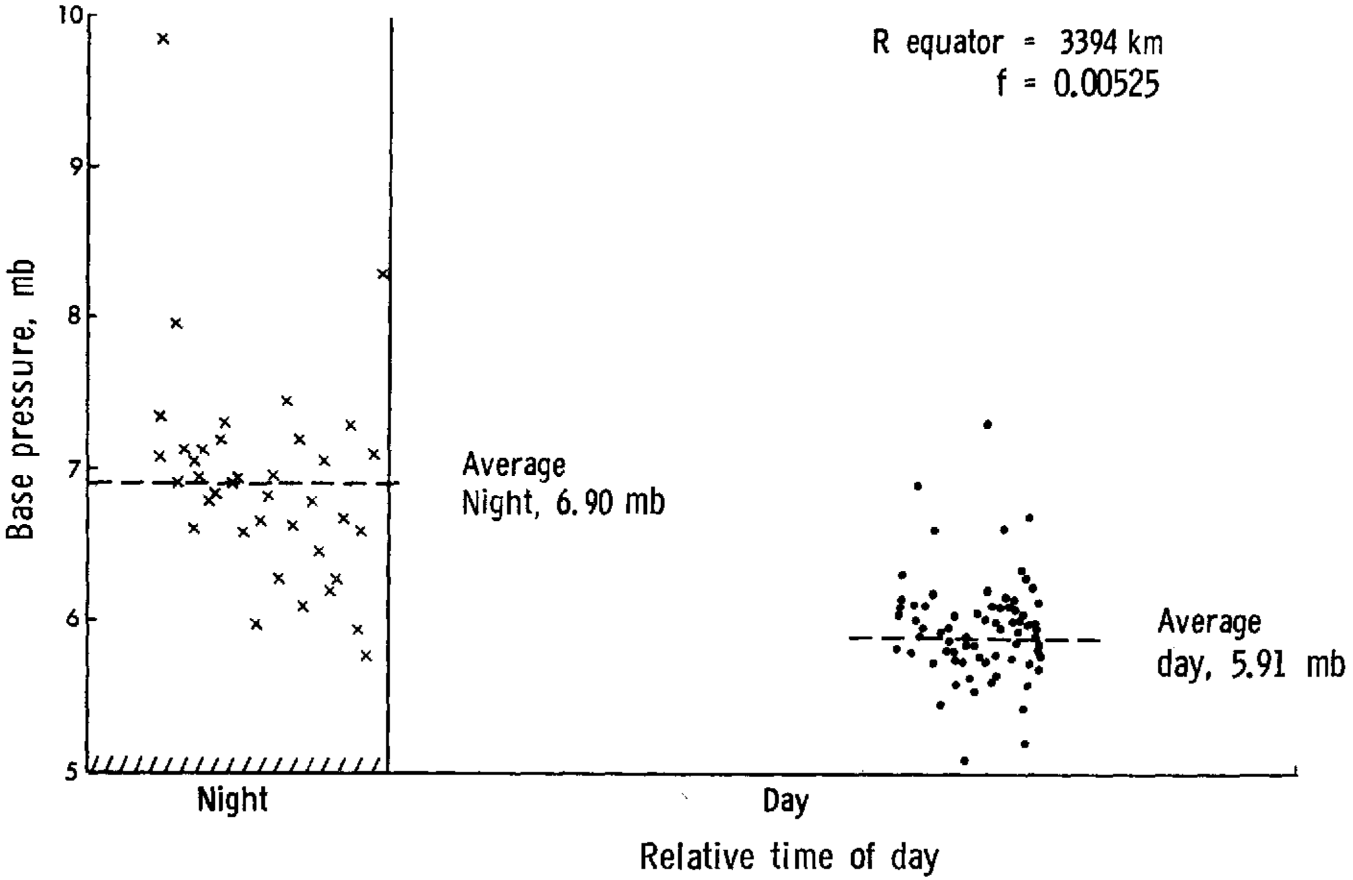

Figure 3.- Martian base pressures from Mariner 9 radio occultation. Values referenced to equipotential surface.

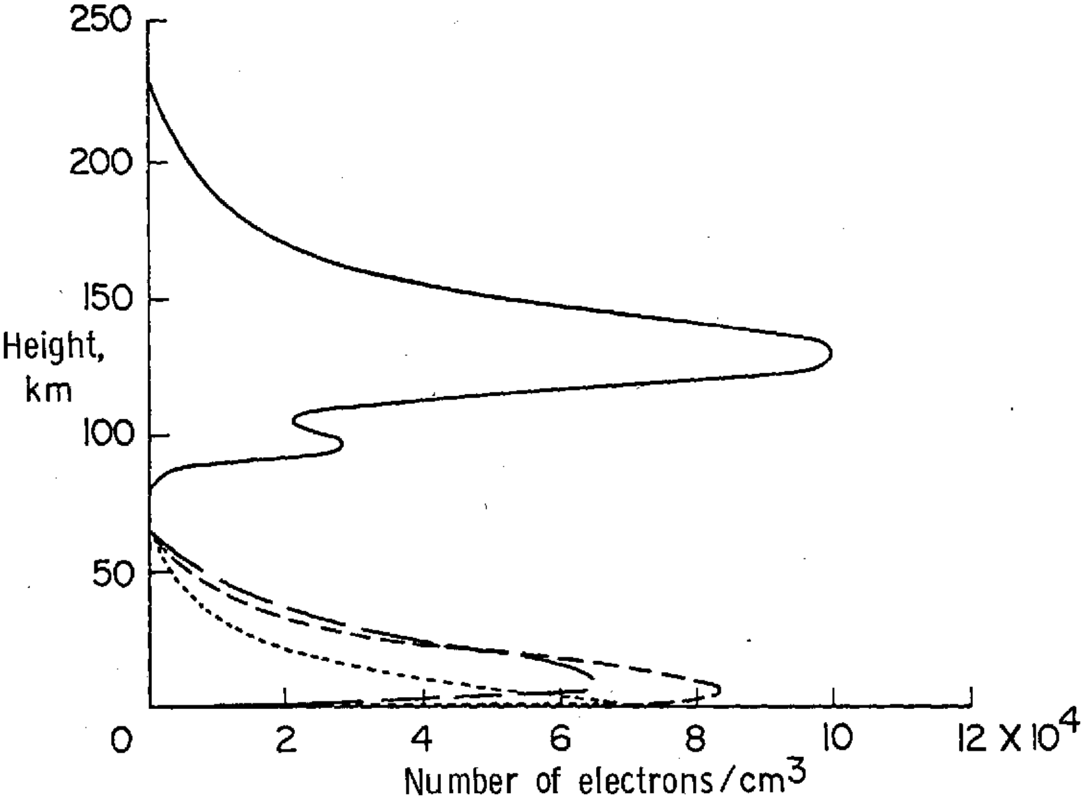

Figure 4.- Calculated lower atmosphere electron density profiles.

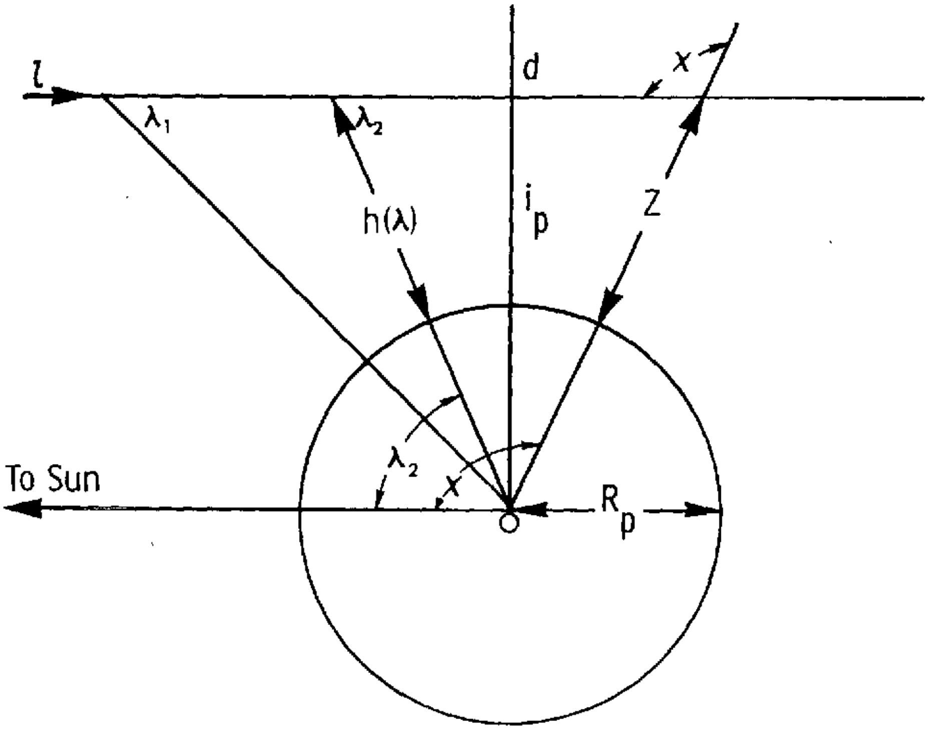

$$i_p = (R+h) = (R+Z)\sin\chi$$

$$l = -i_p \cot\lambda \quad \text{measured from } d$$

$$dl = i_p \csc^2\lambda \, d\lambda$$

Figure 5.- Geometry used in the derivation of electron production equation.

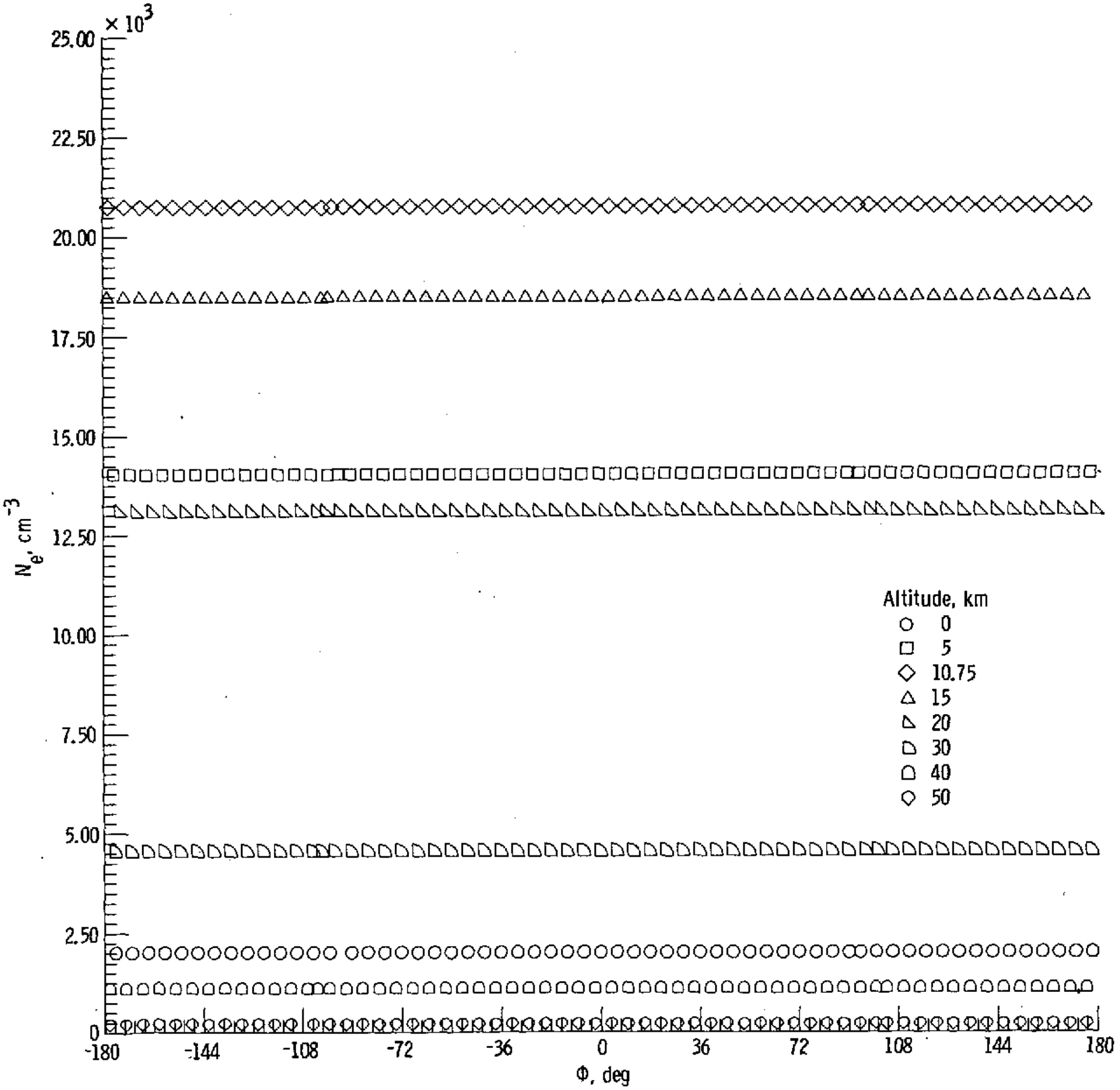

(a) Electron densities as function of hour angle.

Figure 6.- Calculated electron densities for model 0.

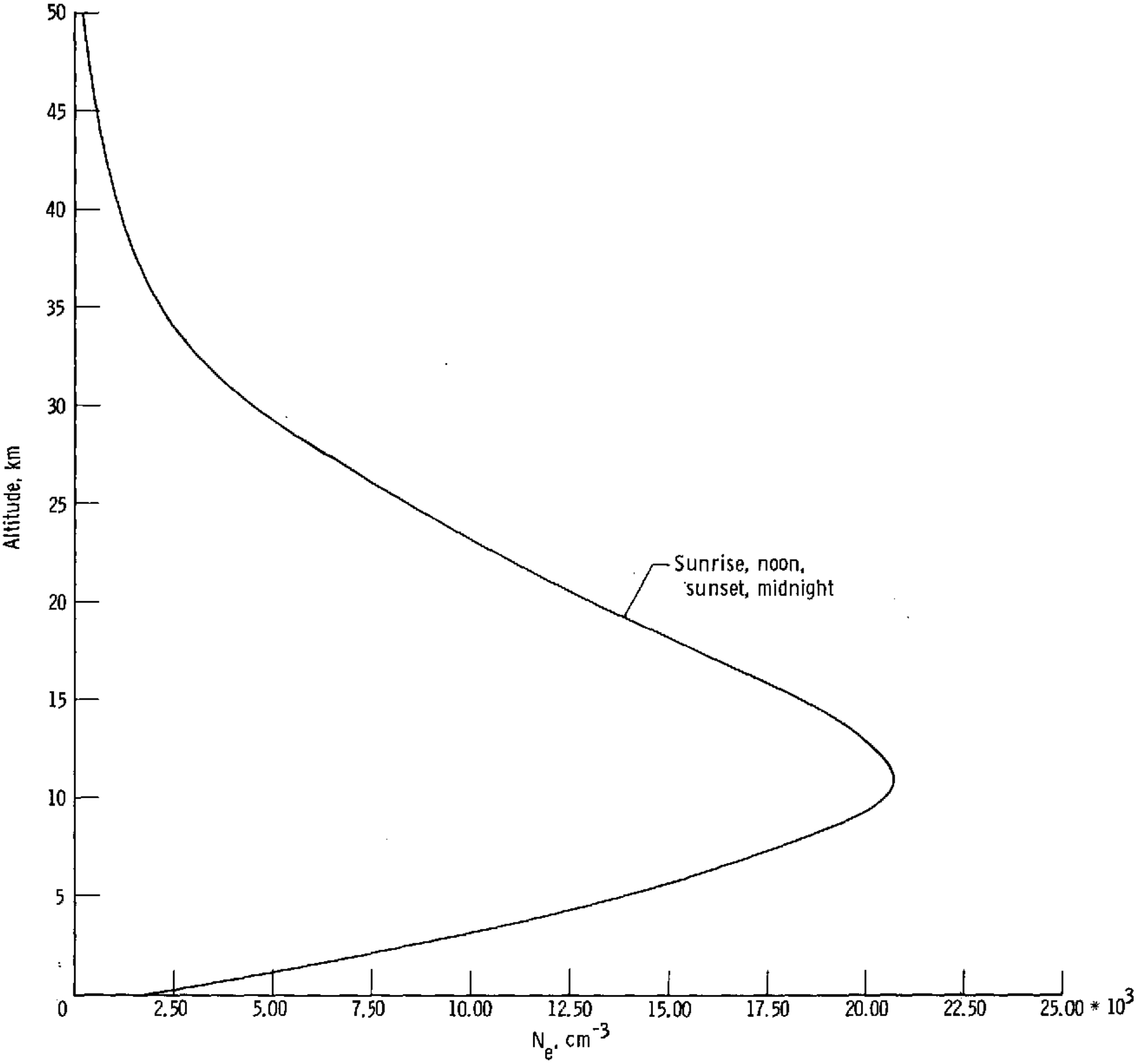

(b) Electron profile.

Figure 6.- Concluded.

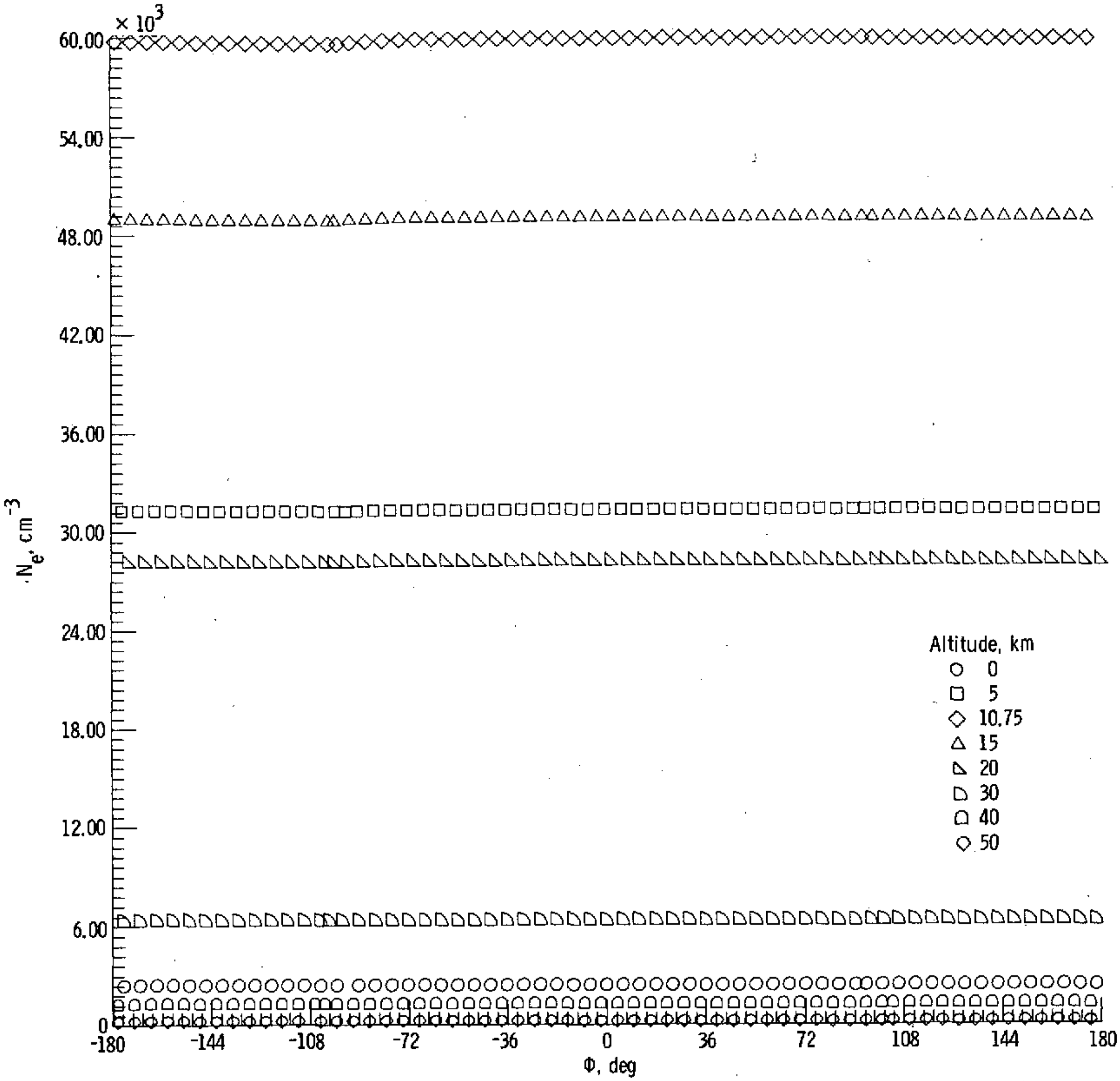

(a) Electron densities as function of hour angle.

Figure 7. - Calculated electron densities for model 1.

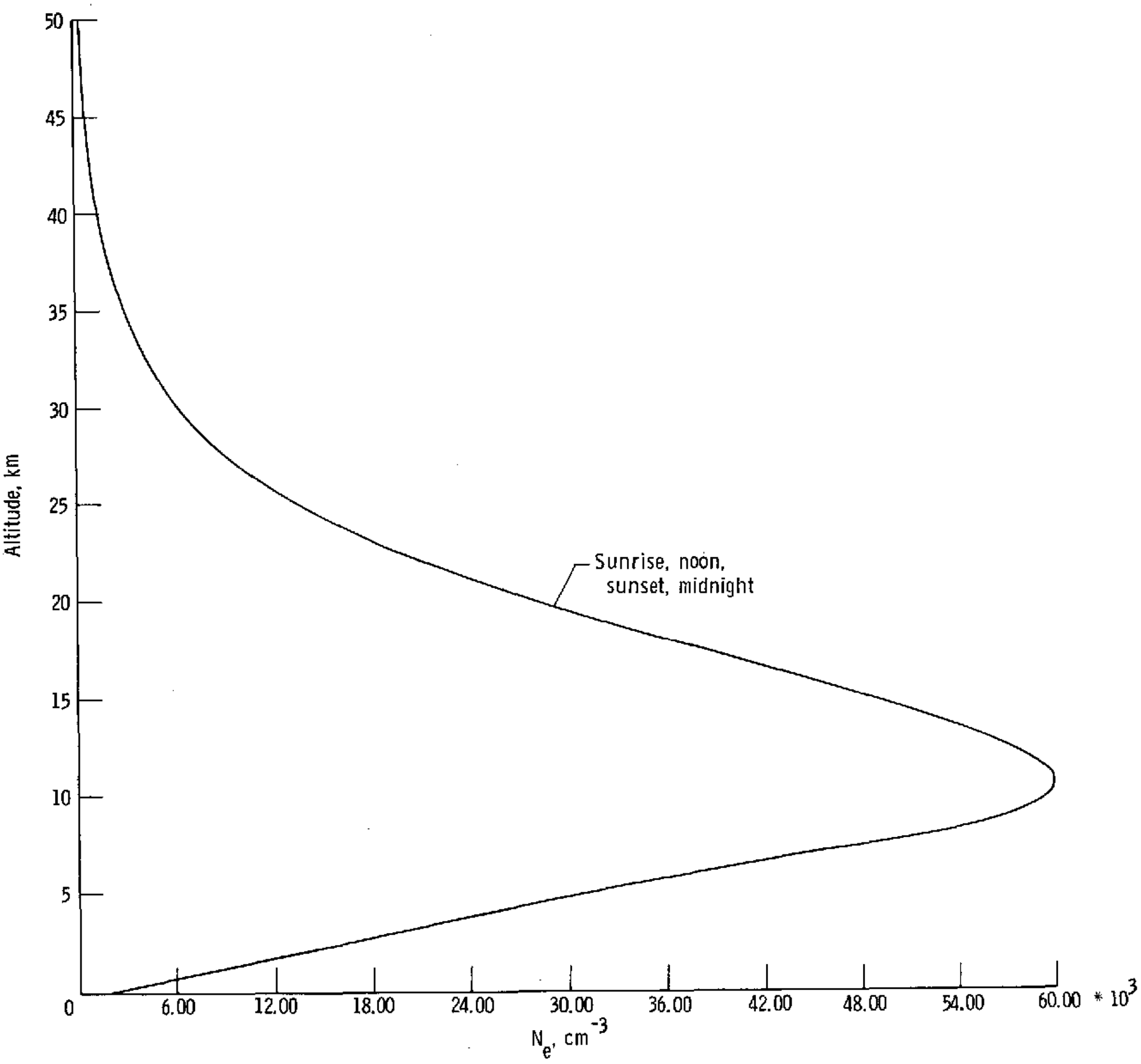

(b) Electron profile.

Figure 7.- Concluded.

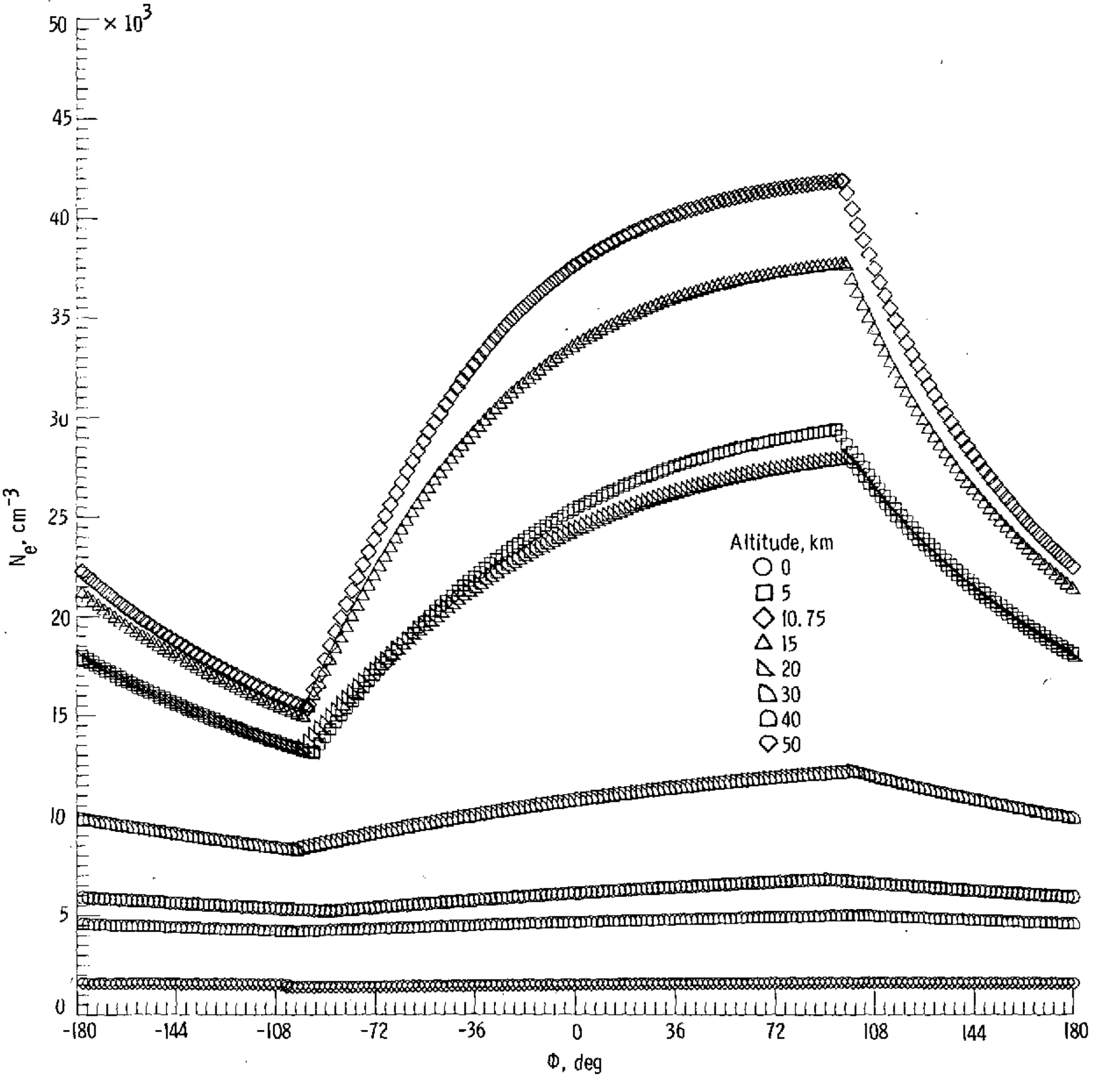

(a) Electron densities as function of hour angle.

Figure 8. - Calculated electron densities for model 2.

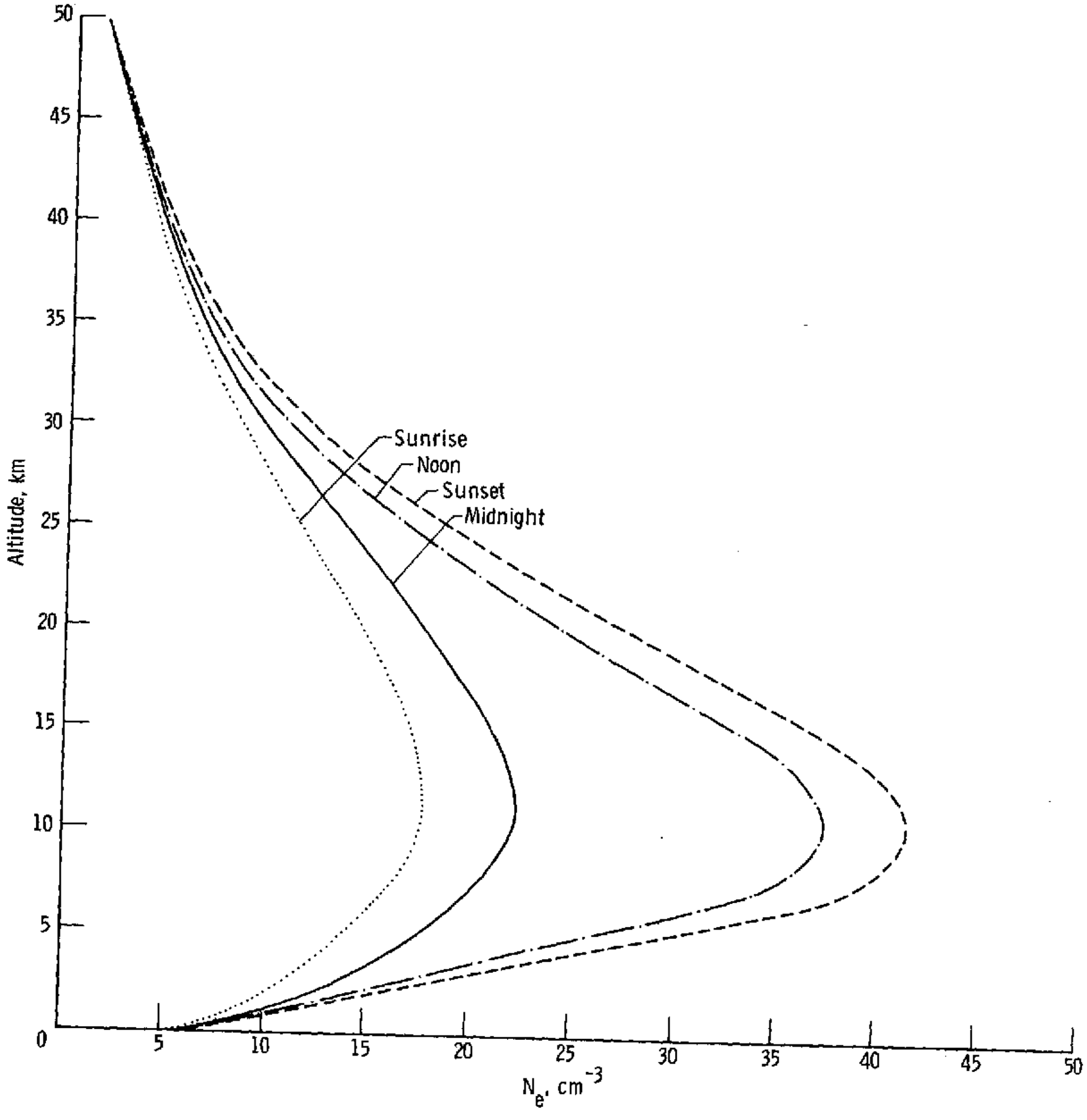

(b) Electron profile.

Figure 8.- Concluded.

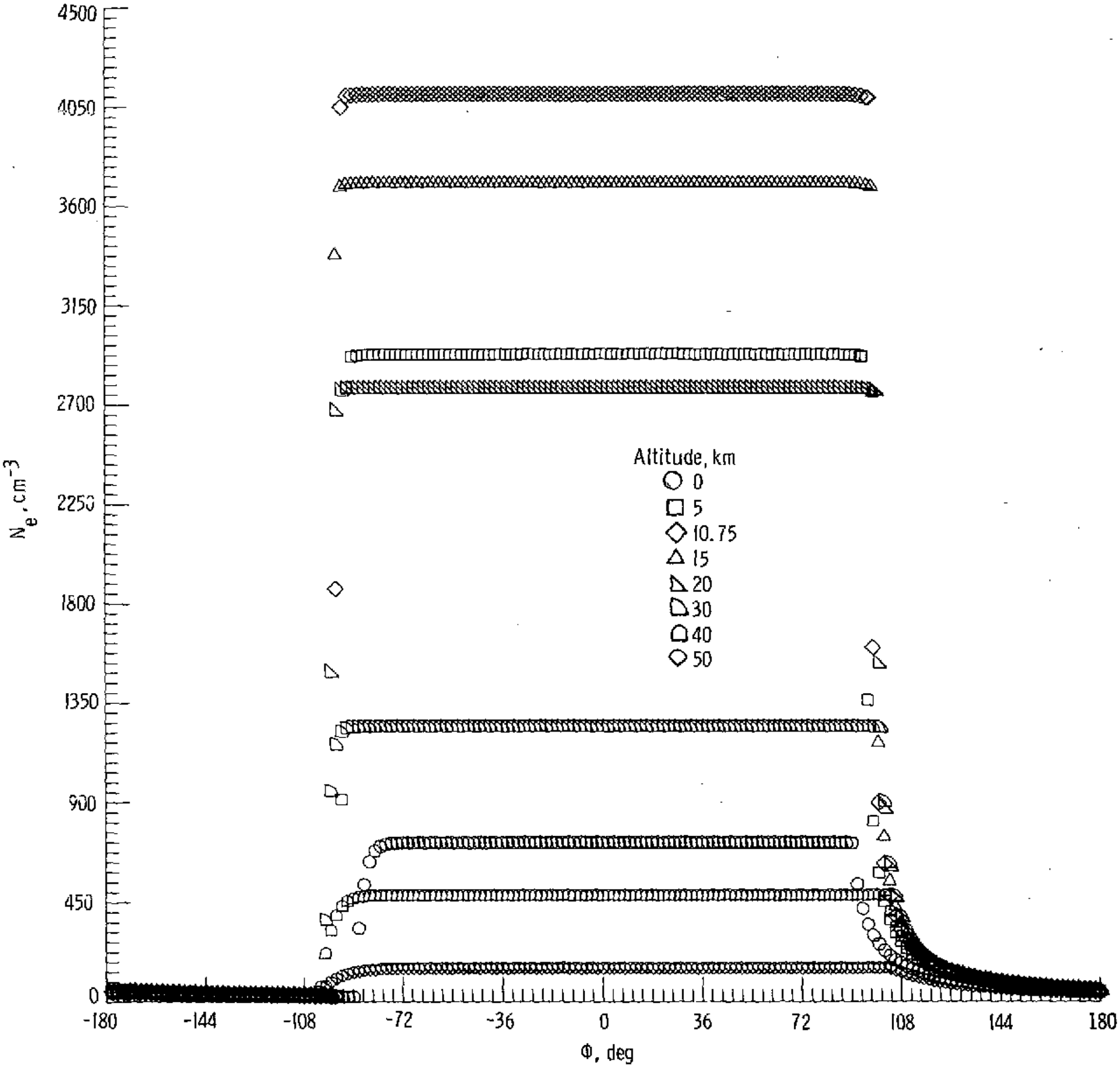

(a) Electron densities as function of hour angle.

Figure 9.- Calculated electron densities for model 3.

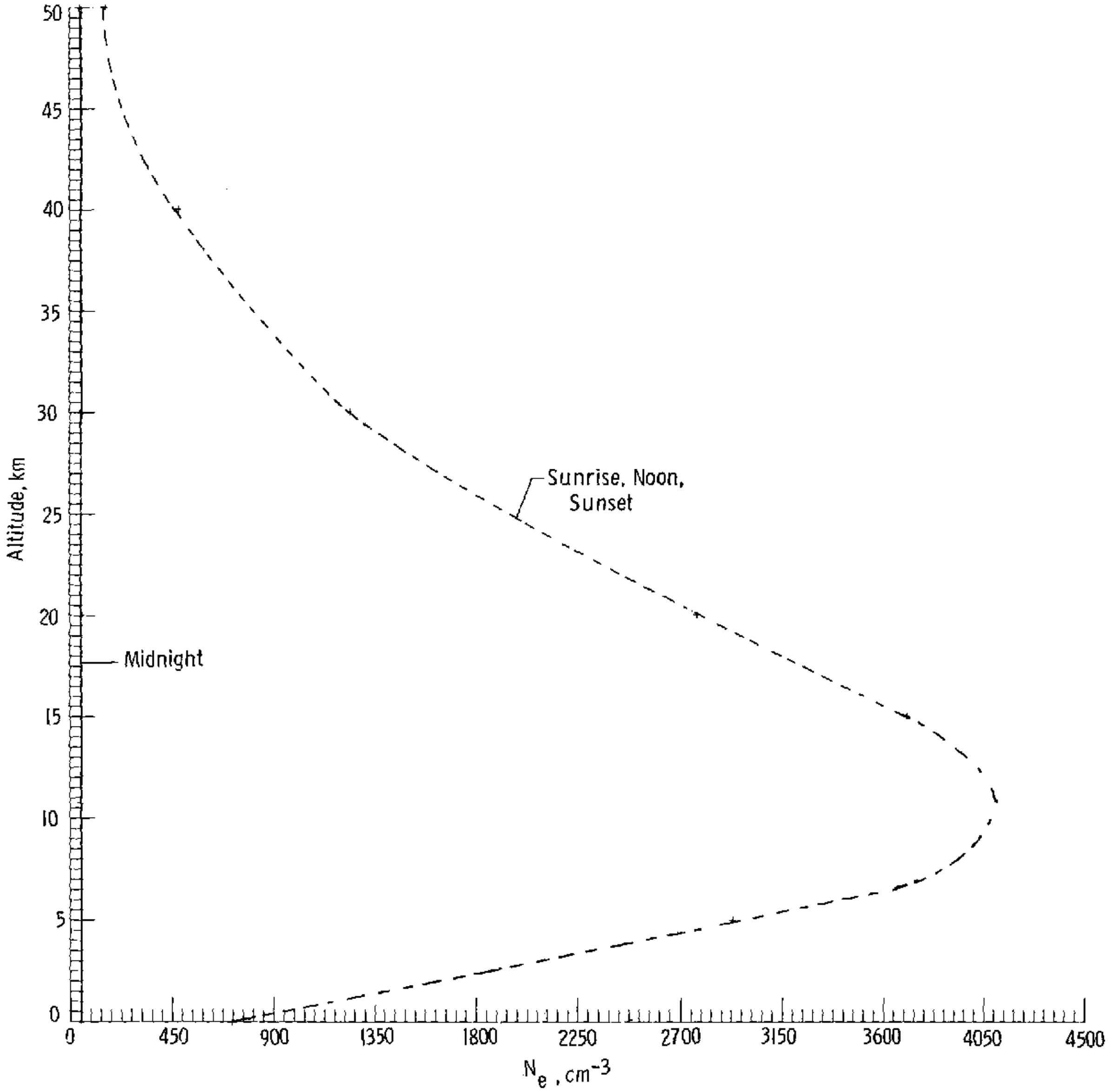

(b) Electron profile.

Figure 9.- Concluded.

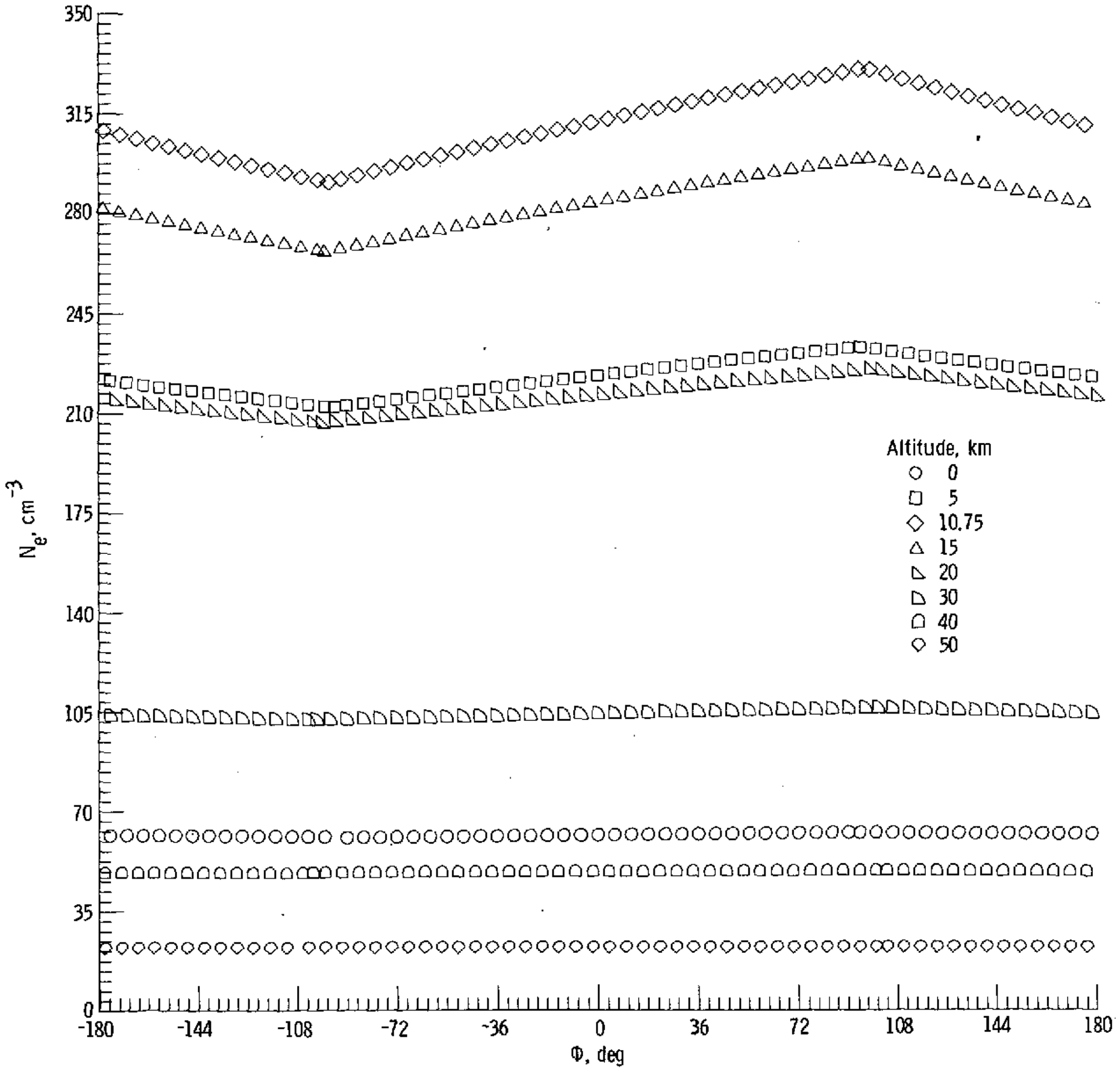

(a) Electron densities as function of hour angle.

Figure 10.- Calculated electron densities for model 6.

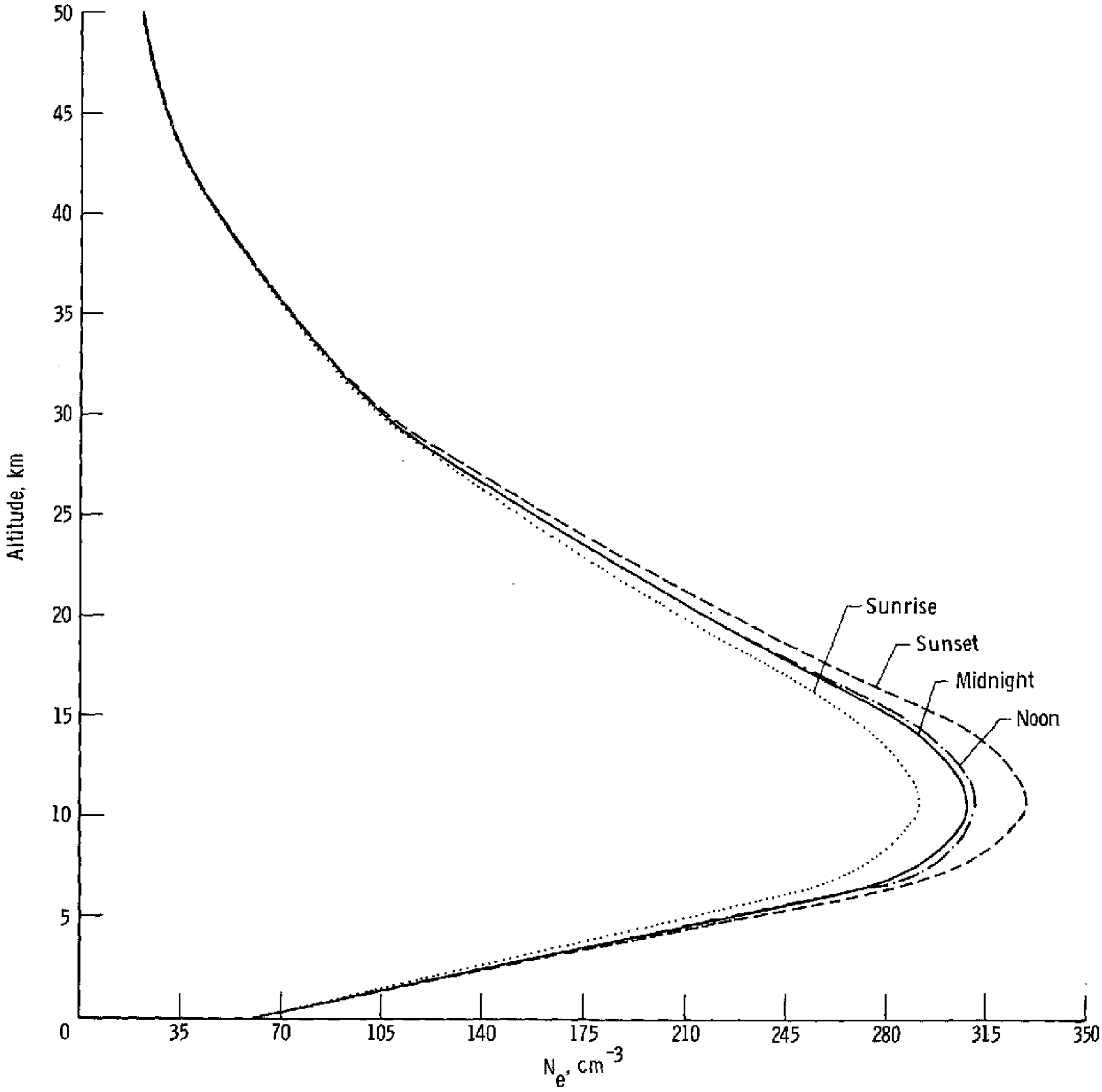

(b) Electron profile.

Figure 10.- Concluded.

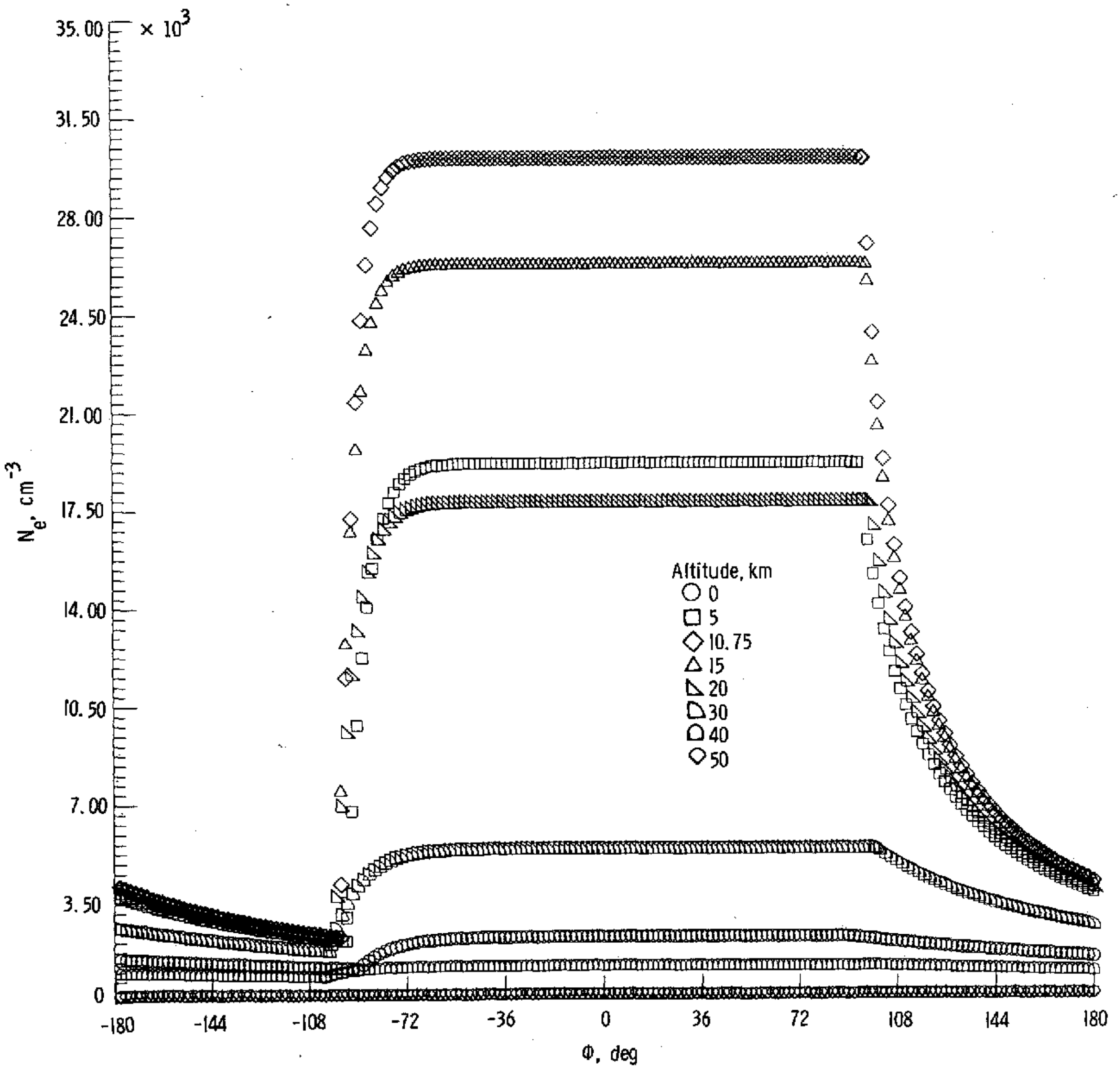

(a) Electron densities as function of hour angle.

Figure 11.- Calculated electron densities for model 7.

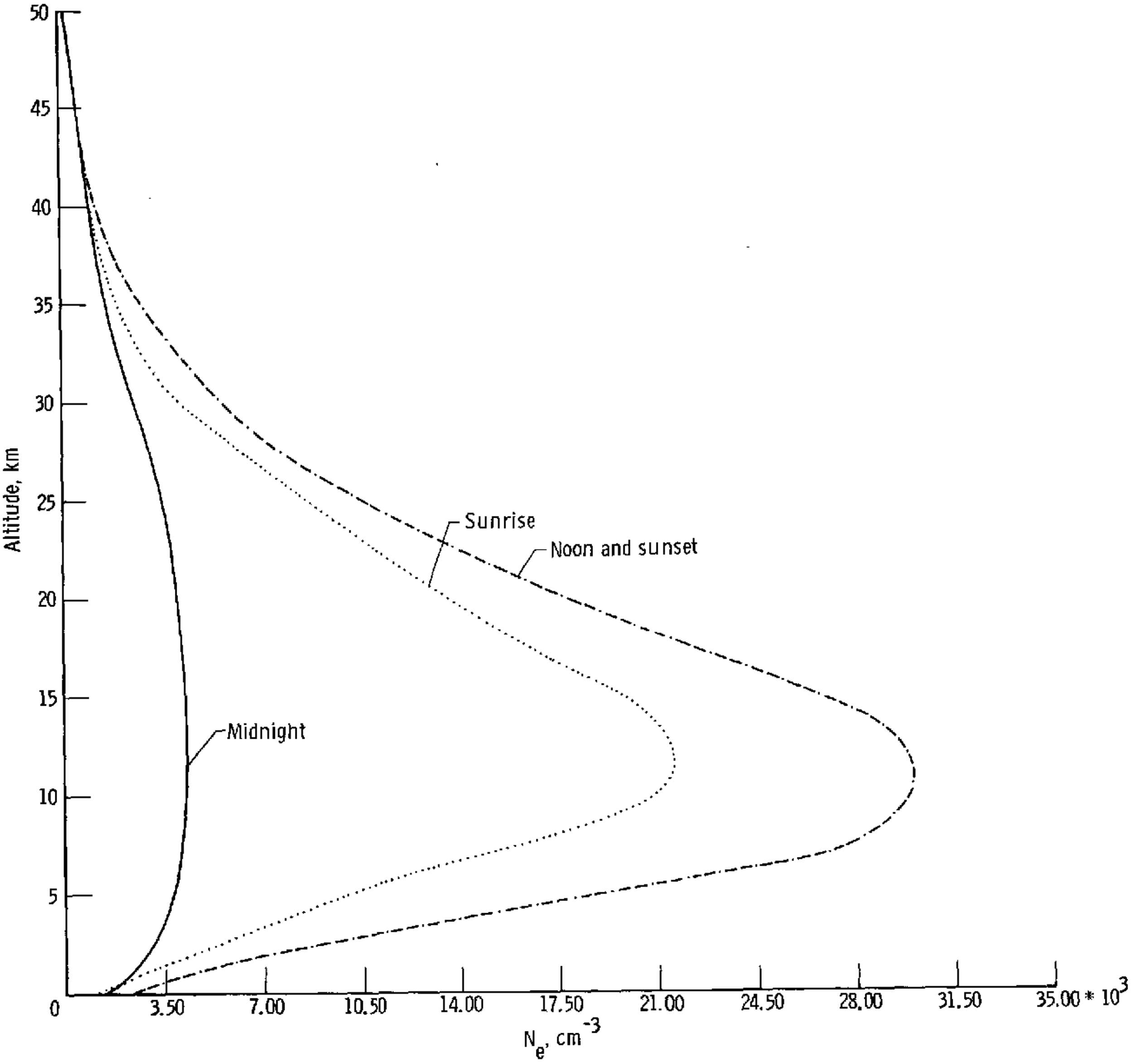

(b) Electron profile.

Figure 11.- Concluded.

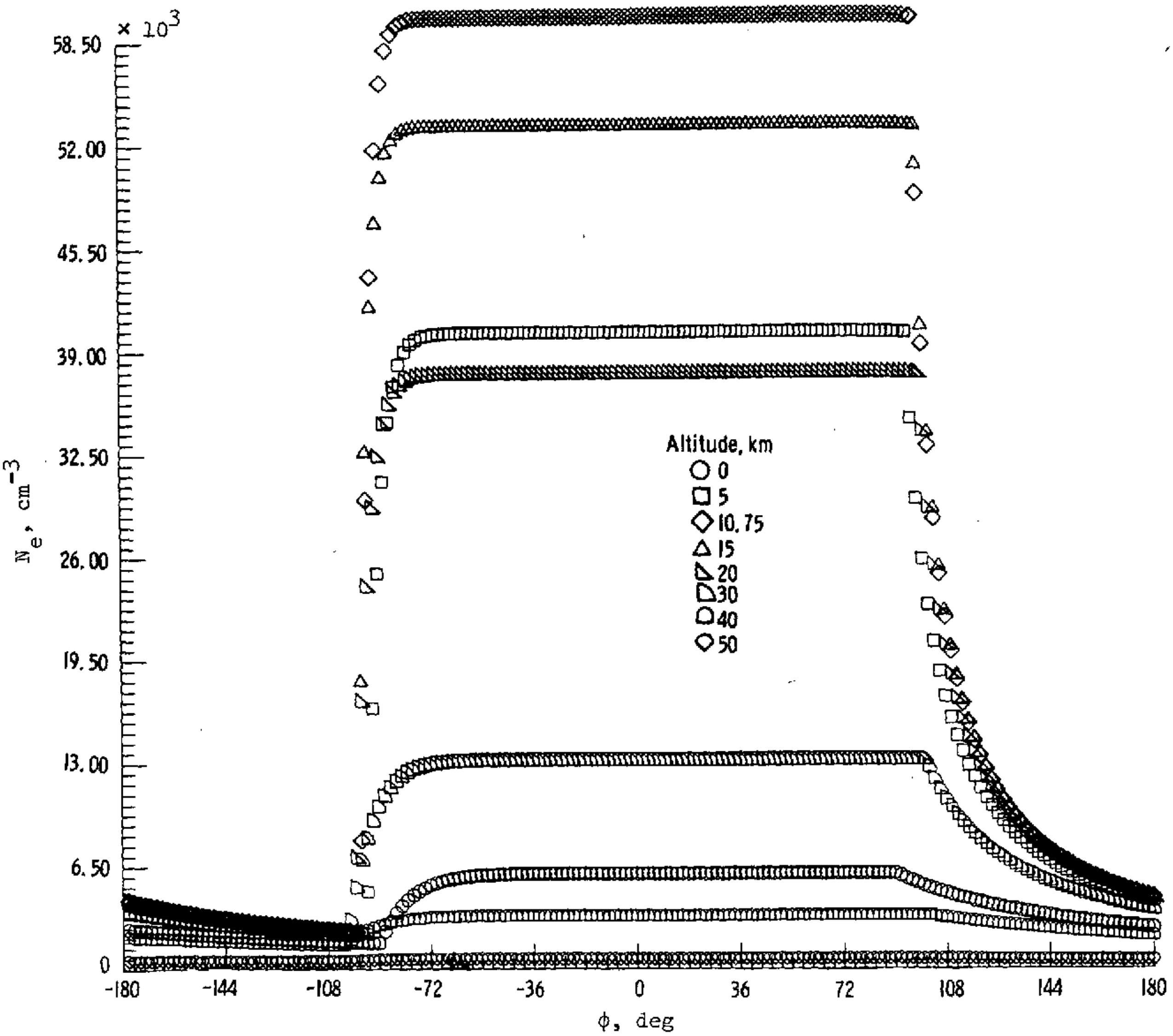

(a) Electron densities as function of hour angle.

Figure 12.- Calculated electron densities for model 8.

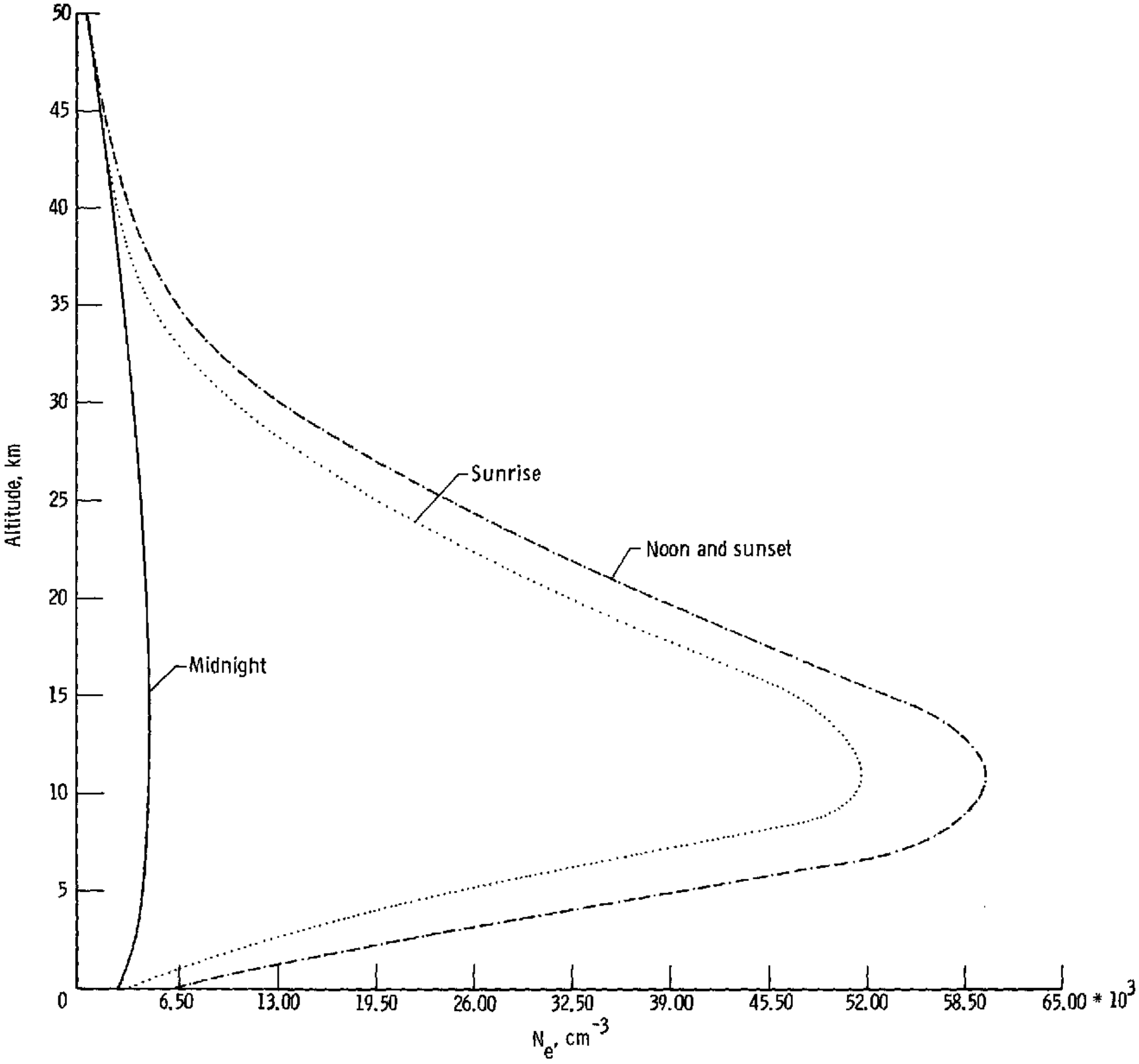

(b) Electron profile.

Figure 12.- Concluded.

NASA-Langley, 1974 L-9600